Saki, M., Thomas, C., Merkel, S., & Wookey, J. (2018). Detecting seismic anisotropy above the 410km discontinuity using reflection coefficients of underside reflections. *Physics of the Earth and Planetary Interiors*, *274*, 170-183. https://doi.org/10.1016/j.pepi.2017.12.001

Peer reviewed version

This is the author accepted manuscript (AAM). The final published version (version of record) is available online via Elsevier at https://www.sciencedirect.com/science/article/pii/S003192011730242X. Please refer to any applicable terms of use of the publisher.

Detecting seismic anisotropy above the 410 km discontinuity using reflection coefficients of underside reflections

Morvarid Saki [a], Christine Thomas [a], Sébastien Merkel [b], James Wookey [c]

[a] Institute of Geophysics, University of Münster

Corrensstr. 24, 48149, Münster, Germany

Author email address: Morvarid Saki: msaki_01@uni-muenster.de, Christine Thomas: cthom_01@ uni-muenster.de

[b] UMET, Unité Matériaux Et Transformations, Bâtiment C6, University of Lille

59650 Villeneuve d'Ascq, Lille, France

Author email address: sebastien.merkel@univ-lille1.fr

[c] School of Earth Sciences, University of Bristol

Queens Road, Clifton BS8 1RJ, Bristol, United Kingdom

Author email address: j.wookey@bristol.ac.uk

Corresponding author: Morvarid Saki

Institute of Geophysics, University of Münster

Corrensstr. 24, 48149, Münster, Germany

Phone: +49 251 8334715

Fax: +49 2518336100

Email address: msaki_01@uni-muenster.de

Abstract

We investigate the effect of various types of deformation mechanisms on the reflection coefficients of P and S waves underside reflections off the 410 km discontinuity, to develop a diagnostic tool to detect the style of deformation at boundary layers. We calculate the reflection coefficient for P and SH underside reflections using velocity perturbations resulting from aligned minerals above the 410 km discontinuity for different deformation scenarios. The results show that in the case of an anisotropic olivine layer above an isotropic wadsleyite layer, the P wave reflection coefficient amplitudes are only slightly influenced by the joint effect of angle of incidence and the strength of imposed deformation, without any polarity reversal and for all deformation styles. For the SH wave underside reflections the incidence angle for which a polarity reversal occurs, changes with distance for all scenarios and in addition changes with azimuth for shear deformation scenarios. These differences in amplitude and polarity patterns of reflection coefficients of different deformation geometries, especially for S wave at shorter distances potentially provide a possibility to distinguish between different styles of deformation at a boundary layer. We also show a first test using currently available elastic constants of anisotropic wadsleyite beneath anisotropic olivine.

Keywords

410 km seismic discontinuity, Underside reflections, Reflection coefficient, Deformation style, Anisotropy

1.Introduction

Seismic anisotropy, the intrinsic property of elastic materials that produces the directional dependence of seismic wave speed and polarization has been observed in many regions of the Earth's interior. A wide range of seismic studies inferred the anisotropic structure of the Earth for example near the surface (e.g., Crampin, 1994) and in the lower crust (e.g., Savage, 1999) and seismic anisotropy in the upper mantle is now well established by SKS splitting and surface waves (e.g., see Yu et al., 1995; Silver, 1996; Montagner, 1998; Savage, 1999; Kendall, 2000; Gaherty, 2004; Long and van der Hilst, 2005; Long, 2009; Eakin et al., 2015). To a lesser extent anisotropy is detected in the lowermost mantle and the D" layer (e.g., Kendall and Silver, 1998; Lay et al., 1998; Ritsema, 2000; Thomas and Kendall, 2002; Nowacki et al., 2010) and in the inner core (e.g., Song, 1996; Morelli et al., 1986; Niu and Chen, 2008; Deuss, 2014).

Seismic anisotropy at mid-mantle depths is not well understood. Indeed, some studies report evidences for little to no anisotropy (e.g., Kaneshima and Silver, 1992; Fischer and Wiens, 1996), while others show the presence of anisotropy on a global scale (e.g., Trampert and van Heijst, 2002; Panning and Romanowicz, 2006) or in the top ~200-250 km of the mantle (e.g., Montagner and Kennett, 1996; Debayle et al., 2005; Yuan and Romanowicz, 2010). In addition, some studies indicate the presence of anisotropy in the mantle transition zone (MTZ) between 410 and 660 km depth (Fouch and Fischer, 1996; Montagner and Kennett, 1996; Beghein and Trampert, 2003; Beghein et al., 2006; Panning and Romanowicz, 2006; Visser et al., 2008; Yuan and Beghein, 2013) as well as below the 660 km discontinuity both regionally (e.g., Tong et al., 1994; Wookey et al., 2002; Chen and Brudzinski, 2003; Wookey and Kendall, 2004) and globally (e.g., Montagner and Kennett, 1996; Trampert and van Heijst, 2002). A mechanism to produce seismic anisotropy is deformation due to mantle flow (see Kendall, 2000 for a review). In this paper, we focus on anisotropy in the upper part of the mantle transition zone and test a method that could potentially be used to detect seismic anisotropy independently of surface waves and shear wave splitting.

The seismic discontinuity at 410 km depth is attributed to a pressure-induced phase transformation of olivine to wadsleyite (e.g., Helffrich and Wood, 1996; Akaogi et al., 1989;

Katsura and Ito, 1989; Katsura et al., 2004). Olivine is volumetrically the most important mineral in the upper mantle. Moreover, olivine-single crystals display a large shear wave anisotropy of up to ~18% (e.g., Mainprice, 2007). Alignment of olivine anisotropic crystals is thus interpreted as the primary source for upper mantle anisotropy (e.g., Kumazawa and Anderson, 1969; Chastel et al., 1993; Abramson et al., 1997; Tommasi, 1998; Stein and Wysession, 2003). Wadsleyite is the high pressure-temperature polymorph of olivine and the primary mantle transition zone mineral constituent between 410 and 520 km depth. Ambient temperature calculations and measurements show that it exhibits a strong intrinsic elastic anisotropy (~10-14% for shear and compressional waves at 410 km depth pressures, e.g., Zha et al., 1997; Mainprice et al., 2000). This anisotropy is stronger than that of ringwoodite and majorite-garnet but weaker than that of olivine (e.g., Pacalo and Weidner, 1997; Sinogeikin et al., 1998; Mainprice et al., 2000).

The presence of anisotropic minerals in the medium does not necessarily produce seismic anisotropy. As suggested by Montagner (1998), four conditions are required in order to detect large-scale mantle LPO (Lattice Preferred Orientation) seismic anisotropy: a) presence of intrinsic anisotropic materials, b) efficient mechanisms of crystals orientation, c) anisotropy of an assemblage of minerals which is usually less than the anisotropy of the pure mineral and d) coherent strain field due to effective deformation field. Anisotropic minerals in the presence of plastic deformation related to mantle flows can potentially develop a Crystallographic Preferred Orientation (CPO) (Karato and Wu, 1993) that gives rise to seismic anisotropy. Due to the direct link between the CPO of mantle minerals and mantle deformation, the study of seismic anisotropy can be used as a marker for the style of mantle flow in different tectonic regions which provides valuable information for our understanding of dynamic processes at depth (e.g., Nicolas and Christensen, 1987; Mainprice and Silver, 1993; Karato et al., 2008; Long and Silver, 2009). However, the interpretation of the MTZ seismic anisotropy in terms of flow geometry is not yet clear, due to little information provided on the CPO of minerals under mantle transition zone pressure and temperature conditions. Furthermore, the interpretation of seismic anisotropy in terms of deformation mechanisms becomes more complicated with the effect of water content of the rocks, deviatoric stress, strain, pressure and temperature on the directional characteristics of anisotropic minerals (e.g., Zhang and Karato, 1995; Bystricky et al., 2000; Zhang et al., 2000; Jung and Karato, 2001a; Durinck et al., 2005; Mainprice et al., 2005; Jung et al., 2006; Katayama and Karato, 2006; Warren and Hirth, 2006; Raterron et al., 2007; Jung et al., 2009; Skemer et al., 2010; Demouchy et al., 2011; Kawazoe et al., 2013; Ohuchi et al., 2014; Raterron et al., 2014).

In addition to the constraints provided by experimental mineral physics, seismological observations and geodynamical modelling, insight into the nature of anisotropic structures in the mantle can be gained by measuring and modelling of reflection coefficients from waves reflected at seismic interfaces (e.g., Thomas et al., 2011). In this study, we extend the method used by Thomas et al. (2011) to establish whether it allows us to detect anisotropy at the 410 km discontinuity. We test whether this approach applied to P and S waves that reflect off the underside of 410 km discontinuity ($P^{410}P$ and $S^{410}S$) potentially provides information on the elastic wave speeds and deformation geometry of the olivine and wadsleyite aggregates deformed by a strain field. Our intent is not to fully cover all the aspects of seismic anisotropy in the mantle transition zone, but rather to provide and test a method that relates PP and SS underside reflections to the style of deformation occurring at the MTZ depths.

2.Methodology

The amplitude and polarity of reflected seismic waves at a given interface are dependent on the impedance (product of velocity and density) contrast between of the two media above and below the interface. A numerical measure of the amplitude and polarity of a reflected wave is given by reflection coefficient and can be computed using Zoeppritz's equations (Zoeppritz, 1919). In the case of isotropic materials the velocities and density do not vary with direction and, as a consequence, the reflection coefficient of the reflected wave does not change as a function of azimuth.

The alignment of anisotropic crystals however, may influence the observed velocities such that the reflection coefficients will vary with azimuth, depending on fast and slow axes of aligned polycrystals. For reflections from the top of the D" layer, Thomas et al. (2011) showed that the azimuthal variations of P and S reflection coefficients can be used as a marker of mineral alignment and the anisotropy above and below the interface.

We compute the reflection coefficients of P and S wave underside reflections using the crystal preferred alignment predictions of olivine produced for different deformation geometries above the 410 km discontinuity. We combine the deformed olivine with non-deformed, isotropic wadsleyite to test whether the reflection coefficient pattern for underside reflections can be used as a diagnostic tool for determining the deformation mechanism occurring at mantle transition zone boundaries (Figure 1). This is the first step, intended to show the validity of the approach but it has to be extended to other cases in the future.

2.1. Elastic constants of single-crystal olivine at high pressure and temperature

The olivine to wadsleyite phase transformation in the average Earth's mantle occurs at pressures around 13.8 GPa (e.g., Bina and Helffrich, 1994) and a temperature of 1760±45 K (e.g., Katsura et al., 2004). The detailed knowledge of the single-crystal elasticity of major mantle minerals such as olivine at relevant pressure-temperature (P-T) conditions is required in order to interpret the observed seismic properties (see Mainprice, 2000 for a review) and especially seismic anisotropy. The elastic moduli of olivine have been investigated at mantle pressures by methods such as impulsive simulated scattering (Abramson et al., 1997), Brillouin scattering (Zha et al., 1996, 1998; Mao et al., 2015; Zhang and Bass, 2016) ultrasonic interferometry (Chen et al., 1996; Liu et al., 2005), and first-principles calculations (e.g., Núñez-Valdez et al., 2013). But, due to experimental and computational difficulties, the full elastic tensor of single-crystal olivine has, to our knowledge, not been provided at simultaneous P and T conditions of the 410 km discontinuity. Mao et al. (2015) used in-situ Brillouin spectroscopy and single crystal X-ray diffraction in externally-heated diamond anvil cells and, reported the elasticity of single-crystal olivine up to 20 GPa and 900 K, which was completed by the study of Zhang and Bass (2016) up to 13 GPa and 1300 K.

In order to obtain the elastic moduli of olivine at P-T conditions relevant to 410 km depth, we compute the P-T derivatives of the elastic constants of olivine by fitting polynomial functions to the experimentally derived elastic moduli reported by Mao et al. (2015). The fitted polynomial functions are characterized by the first order derivative in temperature and second order derivative in pressure. The choice of such polynomials is based on a study by Isaak (1992) which shows that under high-pressure conditions, despite having two different slopes of elastic moduli of olivine versus temperature below and above 800 K, the temperature dependence of C_{ij} can be described by a linear expression. We then extrapolate the polynomial to the relevant pressure of 13.3 GPa and temperature of 1750 K. The obtained values for elastic constants of olivine are listed in Table 1. These values have been used as the olivine single-crystal elastic constants to calculate the polycrystalline elastic properties of olivine and for further calculations of P and S wave reflection coefficients.

It should be noted that the experimental measurements uncertainties of elastic moduli given by Mao et al. (2015) are not taken into account for calculation of P-T derivatives. However, to investigate the possible effect of different elastic moduli values of olivine on the reflection coefficients of P and S waves, a second order polynomial for both pressure and temperature derivatives was also tested. These elastic moduli differ by up to 25 GPa from those of Table 1. Nevertheless, reflection coefficients obtained for P and S waves using this set of elastic constants exhibit a negligible difference compared to those produced from the first set of elastic moduli of olivine and we therefore focus on the results associated with the first class of elastic constants.

2.2. Elastic constants of single-crystal wadsleyite at high pressure and temperature

A number of studies have been carried out to determine the polycrystalline elastic properties of wadsleyite under different pressure and temperature conditions (Li et al., 1998; Li et al., 2001; Mayama et al., 2004; Isaak et al., 2007; Liu et al., 2009; Kawazoe et al., 2013; Núñez-Valdez et al., 2013). However, the single-crystal elasticity of wadsleyite was only evaluated at ambient conditions (Sawamoto et al., 1984; Sinogeikin et al., 1998) and pressures up to 14 GPa at ambient temperature (Gwanmesia et al., 1990; Zha et al., 1997; Wang et al., 2014). Temperature effects on the single crystal elastic moduli of wadsleyite are unknown. Hence, due the lack of published single-crystal elastic properties of wadsleyite at high temperature, we decided to concentrate our analysis on isotropic properties for which the values of bulk and shear moduli are sufficient. We use the adiabatic aggregate bulk (K_s) and shear (G) moduli and their pressure derivatives reported by Wang et al. (2014) for an anhydrous iron-bearing wadsleyite with [Fe]/[Fe+Mg] molar ratio of 0.075, and the temperature derivatives of Mayama et al. (2004). We then derive effective elastic properties for an isotropic aggregate of wadsleyite at the conditions of 410 km depth (Table 1). Finally, note that the elastic parameters we obtain differ from those proposed by Liu et al. (2009) by up to 20 GPa, which is the best resolution one can hope for at present.

2.3. Deformations style

With imposed deformation, crystallites in the polycrystal will orient and generate Lattice Preferred Orientations (LPO), also known as texture. LPO evolution is essentially controlled by the macroscopic deformation, the initial texture, and the active plastic deformation mechanisms (Mainprice et al., 2005).

As mentioned above, we concentrate on cases with anisotropy in the olivine stability field, above 410 km, and isotropy in the wadsleyite stability field, below 410 km. According to experimental data, the olivine to wadsleyite transformation may not preserve LPO across the 410-km discontinuity (e.g., Smyth et al., 2012; Rosa et al., 2016). Indeed, although wadsleyite can nucleate at intracrystalline sites in olivine with well-defined orientation relationships, the lamellae act as nucleation sites for faster-growing incoherent wadsleyite grains with no orientation memory of the parent olivine grains (e.g., Rosa et al., 2016). Thus, in regions of downwelling, assuming LPO in olivine above the 410 km discontinuity and random texture (i.e. isotropy) below the 410 km discontinuity is a proper first-order approximation.

We test two different classes of deformation geometries. First, we test the effect of axial compression applied to the olivine polycrystals above the 410 km discontinuity and the second class includes deformation in shear for both cases where the shear direction is horizontal (parallel to the discontinuity) or vertical (perpendicular to the discontinuity). In each case we assume an isotropic starting texture and let the LPO evolve with the imposed deformation.

2.4. Calculation of olivine LPO

Polycrystal LPO are simulated using polycrystal plasticity simulations utilizing the second-order self-consistent model, initially proposed by Ponte Castañeda (2002) and extended by Detrez et al. (2015). This mean-field micromechanical model accounts for the slip systems at the grain level and an isotropic relaxation mechanism. Olivine is lacking four independent slip systems at the grain level, which is necessary to accommodate any arbitrary plastic deformation in the aggregate. Hence, an additional relaxation mechanism is required but the microscopic origin of this additional relaxation mechanism is not known at this time although it could relate to mechanisms such as grain boundary sliding (e.g., Ohuchi et al., 2015) or disclinations (Cordier et al., 2014). The isotropic mechanism allows removing the fictitious <110>{111} slip system used in previous computations (e.g., Tommasi, 1998; Castelnau et al., 2008). Simulations are performed for a 1000 grains random starting aggregate. In compression, calculations are performed in steps of 1.25% axial strain up to a final strain of 100%. Polycrystal LPO's are saved at the start of the simulation, 25%, 50%, 75%, and 100% axial strain (Figure 2). Shear simulations are run in steps of 2.5% shear, up to a final shear strain of $\gamma = 4$ (400%). Textures are saved at the start of the simulation, and at $\gamma = 1, 2, 3, 4$.

The dominant plastic deformation mechanism of olivine tend to change with the effect of water content, deviatoric stress, pressure and temperature (e.g., Mainprice et al., 2005; Jung et al., 2006; Raterron et al., 2014). Here, we hence design two plastic models for olivine at the conditions of 410 km. The first model is that of Raterron et al. (2014), at the conditions of 405 km, with dominant slip along [001](010) (Table 2). In shear this model leads to B-type textures according to the classification of Jung et al. (2006). The second model is that of Tommasi (1998) with dominant slip on [100](010) (Table 2). In shear this model leads to A-type textures. While the second model is typical for olivine deformed under low stress, low pressure, and low water content conditions the model from Raterron et al. (2014) is appropriate for how we believe olivine behaves deeper in a dry mantle.

A number of studies suggest a different plastic behaviour between hydrous and anhydrous olivine (e.g. Jung et al, 2006, Ohuchi et al, 2017). Ohuchi et al (2017), for instance, showed that hydrous olivine is much weaker than dry olivine and that a significant portion of the strain could be accommodated by dislocation accommodated grain boundary sliding, in conjunction with dominant [100] slip or on the [001](100) slip system. Simulations with dominant [001](100) slip system will result in other elastic constants than the two models above. Investigating this, however, goes beyond the goal of this paper and will require further future investigations.

3. Reflection coefficient modelling across the 410 km discontinuity

For a given deformation style, we calculate the polycrystalline elastic tensor of olivine in the Hill average (Hill, 1952) using the modeled texture and the single crystal elastic moduli of Table 1. Since we use an isotropic model for wadsleyite, the polycrystal elastic tensor is the same as that of the single-crystal. Densities for each phase are taken from the study of Inoue et al. (2004) and are listed in Table 1.

We compute the reflection coefficient of the P and S waves reflected at the underside of the 410 km discontinuity using the anisotropic raytracer ATRAK (Guest and Kendall, 1993) and the matlab toolkit MSAT (Walker and Wookey, 2012). The output of this tool is the velocity perturbations and the reflection coefficients across the discontinuity as a function of azimuth. Reflection coefficients of P and S waves depend strongly on the angle of incidence, i.e., on distance (Zoeppritz, 1919) and should therefore be computed for a range of incidence angles and as a function of azimuth. For each macroscopic deformation style and each olivine plastic model, we start the simulations with a random orientation for both olivine and wadsleyite crystals, and we then increase the alignment of the olivine grains with deformation.

The reflection coefficients for isotropic olivine and wadsleyite are given in Figure 2.e (white circles) as starting texture and the results indicate that the P-wave reflection coefficient is negative for all incidence angles while the SH reflection coefficient is positive for incidence angles smaller than 53 degrees (epicentral distances larger than approx. 39 degrees) and negative for larger incidence angles (epicentral distances smaller than approx. 39 degrees). In the following we focus especially on the results of the reflection coefficients modelling of P and S waves for the cases of axial compression, horizontal shear, and vertical shear and compare the deformed (anisotropic) cases to this isotropic reference case.

4.Results

4.1. Vertical compression

The texture of CPO of olivine induced by the vertical compression is symmetric around the axis of applied deformation (see Figure 2.c). The calculation of P and SH wave reflection coefficients for the axial compression deformation hence leads to reflection coefficients that do not depend on azimuth (Figure 2.d). This is due to the symmetry of the deformation, which induces a symmetry on the polycrystalline texture and a hexagonal symmetry in the polycrystalline elastic tensor, whatever the plastic model used for olivine.

We observe an overall constant negative reflection coefficient for P underside reflections with small amplitude variations depending on the applied deformation intensity for the two plastic models used for olivine and therefore similar to the isotropic reference case. Precursors would therefore have the same polarity as PP waves reflected off the surface. For SH underside reflections the level of applied deformation changes the incidence angle at which the polarity reversal occurs, and generally moves the polarity reversal for the reflection coefficient to larger incidence angles and therefore even shorter epicentral distances (Figure 2.e).

4.2. Horizontal shear deformation

In a second step we investigate shear deformation in the form of horizontal and vertical shear. Figure 3 shows the textures associated with this deformation for two plastic models of olivine based on Tommasi (1998) and Raterron et al. (2014) at 405 km depth, as explained before. While the textures for compression deformation exhibit similar strength for both models (Figure 4), in the case of shear deformation textures resulting from the plastic model of Tommasi (1998) are much stronger than those obtained with the model of Raterron et al. (2014) at 405 km (Figure 3). In both cases, the (010) planes align with the plane of shear. For the model of Tommasi (1998), the [100] directions align sub parallel to the shear direction whereas for the model of Raterron et al. (2014) at 405 km, the [001] directions align sub-parallel to the shear direction.

The results of reflection coefficient modelling for the case of horizontal shear using the B-type slip system (Raterron et al., 2014, 405 km) are described in Figure 5. As before, we vary the incidence angles from 15^o to 65^o (Figure 5) and calculate reflection coefficients for varying azimuths. Since variations of the reflection coefficients of P and SH underside reflections with azimuth are visible (Figure 5.a), we display the reflection coefficients for three different directions: parallel to the direction of deformation (angle of 0 degrees), with an angle of 45 degrees to the direction of deformation and perpendicular to the deformation direction (90 degrees).

Our results for the horizontal shear deformation again show negative P-wave reflection coefficients for the whole range of incidence angles with only slight variations with azimuth for different shear deformation. For the SH wave reflection coefficients we find a more pronounced behaviour: the variations of velocities due to applied deformation leads to a larger variation of the reflection coefficients of the SH wave with azimuth. Compared to the undeformed case we find reduced values in the direction of shear (azimuth of 0 degrees) and elevated values in the azimuth of 45 degrees and to a lesser extent at 90 degrees i.e., perpendicular to shear (Figure 5.a). This anisotropy leads to a change of amplitudes with propagation directions and hence influences the distance at which a polarity reversal occurs for waves reflecting at the same point but in different propagation azimuths (Figure 5.b-d) which is not observed for the compression deformation style. This variation of azimuthally dependent reflection coefficient offers a possibility to test the presence of anisotropy using reflection coefficients of the reflected S waves from the underside of a boundary layer.

Since the polarity change of the SH wave occurs at incidence angles between approximately 40 to 60 degrees (Figure 5), we focus on this distance range to investigate the reflection coefficient of SH waves for two different shear deformations and the two deformation models from the studies of T-98 (Tommasi, 1998) and R-14 (Raterron et al., 2014). Figure 6 shows the results: the reference case (white circles) with the change from positive to negative values for all cases at 39 degrees epicentral distance is given as comparison. For the vertical shear and for both models T-98 and R-14 the polarity reversal distances moves to smaller epicentral distances (larger angles of incidence) while still displaying directional variations. The extreme case is seen for vertical shear and the plastic olivine model T-98, for which the SH reflection coefficient remains positive over the whole range of 40 to 60 degrees 45 degrees away from the shear plane. For horizontal shear and the plastic model R-14, the polarity reversal happens at shorter epicentral distances than the isotropic case 45 degrees away from the shear direction while it does not significantly change in the other orientations. With the plastic model T-98, the polarity reversal is predicted at larger epicentral distance (smaller incidence angles) after shear deformation, which is the opposite of what is predicted for vertical shear. However, keeping in mind that SS underside reflections are usually studied at epicentral distance ranges of over 100 degrees(incidence angle of ~ 42 degrees) (e.g., Chambers et al., 2005; Schmerr and Garnero, 2006; Deuss, 2009; Zheng and Romanowicz, 2012; Saki et al., 2015), the effects that one would measure at these distances would result in amplitude changes with direction only.

5. Discussion

Flow in the mantle, through upwelling plumes and downgoing slabs, deforms mantle minerals and can lead to anisotropic behaviour (e.g., McNamara et al., 2003; Nippress et al., 2004). Detecting and discriminating between different deformation styles may help to distinguish between different styles of subduction and may help to discriminate between slabs stagnating in the mantle transition zone and those that descend into lower mantle (e.g., van der Hilst et al., 1991; Fukao et al., 1992; Fukao and Obayashi, 2013; French and Romanowicz, 2015). Surface wave analysis (e.g., Kawasaki and Kon'no, 1984; Montagner, 1998; Maupin and Park, 2007) and splitting measurements (e.g., Silver and Chan, 1991; Long and van der Hilst, 2005) have been employed to test anisotropy in the upper mantle but here we test another independent method of using body waves that reflect at a boundary layer and use directional variation of reflection coefficients to discriminate between different styles of deformation. Especially at boundary layers, where for example a mineral phase transition is generating reflected waves, this method can potentially provide useful information on anisotropy and deformation.

We test our method on the case of underside reflections generated at the 410 km discontinuity, where the phase transition from olivine to wadsleyite occurs. In the layer above the discontinuity we use deformed olivine. Investigating anisotropy in the mantle transition zone, however, has to be carried out with detailed knowledge of the evolution of the LPO of polycrystalline olivine with increasing pressure and temperature simultaneously with the available elastic moduli of single crystal olivine (Mainprice et al., 2000; Mainprice, 2007). The LPO, slip systems, and plastic mechanisms of olivine, are difficult to study at deep mantle pressures and remain a matter of current debates (e.g., Jung and Karato, 2001a; Couvy et al., 2004; Katayama et al., 2004; Faul et al., 2011; Ohuchi et al., 2011; Hilairet et al., 2012; Ohuchi et al., 2015; Bollinger et al., 2016). The choice of a dominant slip system may hence change in future works and influence the results of the reflection coefficient modelling in our study. Here, this effect has been investigated by testing two different plastic models of olivine, as suggested by Tommasi (1998) and Raterron et al. (2014).

To test the feasibility of our method and for the simplest model, we have assumed wadsleyite to be isotropic. Some studies have discussed CPO of deformed wadsleyite (e.g., Demouchy et al., 2011; Kawazoe et al., 2013) and the nature of its dominating plastic mode (e.g., Thurel et al., 2003b; Ritterbex et al., 2016) that may contribute to transition zone anisotropy (Mohiuddin et al., 2015) and early experiments showed that wadsleyite may form a lattice preferred orientation (e.g., Thurel et al., 2003a; Tommasi et al., 2004). From a microscopic point of view, phase transformations can occur through two families of mechanisms, leading to coherent or incoherent orientations between the parent and daughter phases. Smyth et al. (2012) suggested that wadsleyite CPO can be partially inherited from pre-transformation olivine textures. Dissimilar to coherent orientation of the parent and daughter, loss of anisotropy through transformation is also discussed previously (e.g., Campbell, 2008), but since the elastic constants of wadsleyite at temperature and pressure corresponding to 410 km depth are currently not available for high shear strain, this type of transformation is difficult to test in our study. The only published values to our knowledge are by Kawazoe et al., (2013) with a shear strain of $\gamma = 0.4$.

Assuming wadsleyite to be anisotropic would offer the case of having two anisotropic layers one above and one below the 410 km discontinuity, but it would present a much more complicated first model. To make significant changes to the reflection coefficient, the alignment of wadsleyite would have to combine with the alignment of olivine to generate a reduction in velocity for one direction, which would result in a polarity change for all distances in this azimuthal direction.

Although the elastic constants of wadsleyite at pressure and temperature conditions of the 410 km depth and at high shear strain are not available, we conduct a first test here and use values provided in the literature (Kawazoe et al., 2013).They provide a table with a set of polycrystalline elastic moduli for plastically deformed wadsleyite at 17.6 GPa, 1800 K, and gamma = 0.4. Note, however, that these elastic moduli were not measured at 17.6 GPa and 1800 K. This set of elastic moduli was calculated based on the textures measured after deformation at 17.6 GPa and 1800 K and the single-crystal elastic constants measured by Zha et al (1997) at 14.2 GPa and room temperature. The effect of temperature on elasticity is, hence, not accounted for, possibly leading to a strong over-estimate of all elastic moduli and in particular for C11, C22, and C33. However, in the absence of other results on anisotropic wadsleyite at pressures and temperature of the 410 km discontinuity, we test this case to show the effect it has in our models. The results of the reflection coefficient modelling using this set of elastic constants are shown in Figure 7.

We find that the changes in the S-wave reflection coefficient are similar to the ones for isotropic wadsleyite but the place where the polarity reversal happens occurs at longer epicentral distances. The P-wave polarity, however, changes sign for this case, which perhaps could be due to the larger elastic moduli C11, C22 and C33. More test with anisotropic wadsleyite to understand the effects on P-wave reflectivity will be necessary in the future, when more data on anisotropic wadsleyite become available.

For the simplest setup model including isotropic wadsleyite, we chose the case of anhydrous iron-bearing wadsleyite in our study. Due to the high water storage capacity of wadsleyite up to 0.9%, water can be contained at 15 GPa and 1400^{o}C (Demouchy et al., 2005), and it should be regarded as a parameter which may influence the elastic properties of wadsleyite. The effect of hydration on the elastic constants of wadsleyite is reported at ambient and high pressure conditions (e.g., Mao et al., 2008a, b). However, the existence of a significant water reservoir in the mantle is still a matter of debate. In addition, the presence of a considerable amount of iron in all upper mantle minerals has been shown (Agee, 1998) and large number of studies have discussed the effect of Fe on the elasticity of olivine and wadsleyite (e.g., Duffy et al., 1995; Zha et al., 1996; Núñez-Valdez et al., 2011). For future work, cases with hydrous wadsleyite and varying amounts of iron would be useful.

Results from our reflection coefficients modelling for P and SH waves at the underside of the interface between ansiotropic olivine and isotropic wadsleyite exhibit different pattern, depending on the applied deformation geometry on olivine. Our modelling shows that different deformation geometries do not create large amplitude variations for P wave reflections. The reflection coefficient of underside reflections of P wave always exhibits negative polarities without any polarity reversal for all tested deformation geometries. However, the assumption of inheriting anisotropy through olivine-wadsleyite phase transition for a horizontal shear deformation would likely change the results. In Figure 7, we do observe polarity reversal of the P wave reflection coefficients at epicentral distances around 75 degrees but more work is needed to constrain this effect with elastic constants of anisotropic wadsleyite measured at conditions of the mantle transition zone. Some polarity changes of PP underside reflections have been observed in previous studies (e.g., Courtier and Revenaugh, 2007; Jasbinsek and Dueker, 2007; Thomas and Billen, 2009; Schmerr and Thomas, 2011) and previous suggestions for these polarity reversals include melt or metastable olivine wedges, but no conclusive interpretation has been given so far. Results from our modelling suggest that anisotropy in the olivine layer in combination with isotropic wadsleyite is likely not the cause for the observed polarity changes in PP precursors, however, more complicated models with anisotropic wadsleyite could potentially explain the polarity reversal of PP waves.

The results of reflection coefficient modelling for SH wave show variations of the epicentral distance, where the sign of the reflection coefficients of SH underside reflections at the 410 km discontinuity occurs. This effect is independent of having isotropic or anisotropic wadsleyite below the 410 km boundary. However, the case of deformed wadsleyite with shear strain of 0.4 shifts the epicentral distances range of polarity reversal to larger values (Figure 7). For the compressional geometry we find that the polarity reversal for the reflection coefficients of the SH wave changes with the percentage of applied compression but not with direction. For both horizontal and vertical shear deformations, however, the azimuth to the direction of imposed deformation plays an important role for the distance where the polarity of the reflected S wave changes sign, independent of the choice of the olivine dominant slip system (Figure 6). This provides a distinct difference between compression and shear deformation geometry and can act as discriminating factor for the detection of the style of deformation system at a boundary layer.

Testing the results of our study with seismological data would provide direct information on deformation for different regions in the Earth, specifically at boundary layers. Modelling results for waves reflected at the D'' layer (Thomas et al., 2011) showed that P and S waves varied strongly in amplitude and also polarity and a combination of both P and S waves is necessary to distinguish between different scenarios. In our study, the combination of anisotropic olivine and wadsleyite produces considerable effect on the behavior of the reflection coefficients of the P waves. While for the case of undeformed wadsleyite the P wave reflection coefficients show only small amplitude variations, anisotropic wadsleyite leads to a polarity reversal of the reflection coefficients at epicentral distances of about 70 degrees. The S wave reflection coefficients change amplitude and the distance at which a polarity reversal occurs for both cases of deformed and undeformed wadsleyite but at larger epicentral distances for the deformed wadsleyite case. Alsodifferent deformation styles shift the place, where polarity reversals of the reflection coefficient in SS waves occur, to shorter epicentral distances than the isotropic case except for the case of the T-98 model and horizontal shear where the polarity reversal occurs between 53 and 44 degrees epicentral distance.

PP and SS underside reflections are generally studied in a distance range over 80 degrees (e.g., Shearer, 2000; Deuss, 2009; Saki et al., 2015). Here we would need SS underside reflections in a distance range of 30 to 40 degrees. While these reflections are in principle possible, the wavefield exhibits triplications in this distance range, making the use of SS underside reflections more difficult. In addition, the reflection coefficient is very small in the vicinity of the polarity reversal and the waves would be difficult to observe in real data. When using a deformed wadsleyite layer below an anisotropic olivine layer shifts the epicentral distance of polarity change range to higher values (~ 50-65 degrees) even for a small shear strain of 0.4 for wadsleyite. Considering deformed wadsleyite with high shear strains may therefore improve our results in terms of the epicentral distance range where the polarity reversal occur. While 65 degrees is still a low distance range for observing SS underside reflections, we show that it is in principle possible to detect S wave underside reflections off the 410 km boundary at epicentral distance between 50 to 60 degrees (Figure 8). The vespagram (e.g., Rost and Thomas, 2002) generated from synthetic seismograms shows a clear S410S (including its depth phase) while the S660S precursor is partly interfering with the S coda.

Even with the current limitations of the setup of our modelling, this study shows the possibility of using the azimuthal dependence of reflection coefficients of the SH underside reflections to study the deformation at the mantle transition zone boundaries. Our results, however, motivate further research of reflection coefficient modelling including an anisotropic wadsleyite layer with higher shear strain,effects of water and also extending the modelling to the discontinuity at 660 km depth. While PP underside reflections off the 660 km discontinuity are less well observed (e.g., Estabrook and Kind, 1996; Deuss, 2009; Thomas and Billen, 2009; Schmerr and Thomas, 2011; Lessing et al., 2014; Saki et al., 2015), SH underside reflections of the 660 km discontinuity are generally visible (e.g., Flanagan and Shearer, 1998; Schmerr and Garnero, 2006; Gu et al., 2012) and our modelling so far suggests that the SH underside reflections are mostly affected by the deformation. Comparison of the calculated reflection coefficients with suitable seismic data would provide further insight into the mantle transition zone mineralogy and deformation and the mechanisms responsible for waveform changes of underside reflections.

6. Conclusions

To study possible processes that may affect the polarity and amplitude variation of the underside reflections off the 410 km discontinuity, we model the reflection coefficients of P and SH waves reflected off an olivine-wadsleyite phase transition. We tested different deformation geometries including axial compression perpendicular to the boundary and shear deformations. For each, we calculate the reflection coefficients for incidence angles ranging from 15 to 65 degrees and all azimuths. The results indicate that P wave reflection coefficients always show negative values without any polarity reversal and with only weak variations in amplitude with the type and strength of applied deformation. The SH wave reflection coefficient for underside reflection undergoes a polarity reversal in the isotropic case, this polarity reversal is shifted to different epicentral distances when olivine is plastically deformed above the boundary. For shear deformation, the angle of incidence, i.e. the distance where the polarity reversal occurs changes also with azimuth. This can serve as discriminating factor and allows this method to be used as a diagnostic tool for identifying the style of deformation at boundary layers. For all deformation styles tested here the polarity change of SH waves occurs at short epicentral distances which are currently not used to investigate upper mantle discontinuities. Further work needs to be carried out for two anisotropic layers, however, the lack of published single-crystal elasticity of wadsleyite at pressures and temperatures of the 410 km discontinuity is a strong limiting factor at the moment. As a first test, using published elastic parameters of wadsleyite shows that the effect of distance dependence for SH waves remains and shifts to larger epicentral distances while the P wave reflection coefficient also shows a polarity reversal. Further extension of the method to the 660 km discontinuity will help to better understand mantle dynamics and slab descend.

Acknowledments

The authors would like to thank the Editor Vernon Cormier and two anonymous reviewers for the helpful comments that improved the quality of this manuscript. Data were analysed using Seismic Handler (Stammler, 1993). The work has been supported by the grant TH1530/10-1 of the Deutsche Forschungsgemeinschaft (DFG).

References

Abramson, E.H., Brown, J.M., Slutsky, L.J., and Zuag, J. (1997). The elastic constants of San Carlos olivine to 17 GPa. J. Geophys. Res.-Solid Earth, 102(B6): 12253-12263.

Agee, C.B. (1998). Phase transformations and seismic structure in the upper mantle and transition zone. In: Hemley, R.J. (Ed.), Ultrahigh-pressure Mineralogy, Mineral. Soc. Am. Rev., 37:165-203.

Akaogi, M., Ito, E., and Navrotsky, A. (1989). Olivine-modified spinel-spinel transitions in the system Mg_2SiO_4-Fe_2SiO_4: Calorimetric measurements, thermochemical calculation, and geophysical application. J. Geophys. Res.-Solid Earth, 94(B11): 15671-15685.

Beghein, C. and Trampert, J. (2003). Probability density functions for radial anisotropy: implications for the upper 1200 km of the mantle. Earth Planet. Sci. Lett., 217(1-2): 151-162.

Beghein, C., Trampert, J., and van Heijst, H.J. (2006). Radial anisotropy in seismic reference models of the mantle. J. Geophys. Res.-Solid Earth, 111(B2). Doi: 10.1029/2005JB003728.

Bina, C.R. and Helffrich, G.R. (1994). Phase transition Clapeyron slopes and transition zone seismic discontinuity topography. J. Geophys. Res.-Solid Earth, 99(B8): 15853-15860.

Bollinger, C., Raterron, P., Castelnau, O., Detrez, F., and Merkel, S. (2016). Textures in deforming forsterite aggregates up to 8 GPa and 1673 K. Phys. Chem. Min., 43(6): 409-417.

Bystricky, M., Kunze, K., Burlini, L., and Burg, J.P. (2000). High shear strain of olivine aggregates: rheological and seismic consequences. Science, 290: 1564-1567.

Chambers, K., Deuss, A., and Woodhouse, J.H. (2005). Reflectivity of the 410-km discontinuity from PP and SS precursors. J. Geophys. Res., 110(B02301). Doi: 10.1029/2004JB003345.

Campbell, F.C. (2008). Elements of metallurgy and engineering alloys, Chapter 4, introduction to phase transformations: 53-61. ASM international.

Castelnau, O., Blackman, D.K., Lebensohn, R.A., and Castañeda, P.P. (2008). Micromechanical modeling of the viscoplastic behavior of olivine. J. Geophys. Res., 113(B09202). Doi: 10.1029/2007JB005444.

Chastel, Y.B., Dawson, P.R, Wenk, H.-R., and Bennett, K. (1993). Anisotropic convection with implications for the upper mantle. J. Geophys. Res.-Solid Earth, 98(B10): 17757-17771.

Chen, W.-P. and Brudzinski, M.R. (2003). Seismic anisotropy in the mantle transition zone beneath Fiji-Tonga. Geophys. Res. Lett., 30(13). Doi: 10.1029/2002GL016330.

Chen, G., Li, B., and Liebermann, R.C. (1996). Selected elastic moduli of single-crystal olivines from ultrasonic experiments to mantle pressures. Science, 272: 979-980.

Cordier, P., Demouchy, S., Beausir, B., Taupin, V., Barou, F., and Fressengeas, C. (2014). Disclinations provide the missing mechanism for deforming olivine-rich rocks in the mantle. Nature, 507: 51-56.

Crampin, S. (1994). The fracture criticality of crustal rocks. Geophys. J. Int., 118(2): 428-438.

Courtier, A.M., and Revenaugh, J. (2007). Deep upper-mantle melting beneath the Tasman and Coral Seas detected with multiple ScS reverberations. Earth Planet. Sci. Lett., 259: 66-76.

Couvy, H., Frost, D., Heidelbach, F., Nyilas, K., Ungar, T., Mackwell, S., and Cordier, P. (2004). Shear deformation experiments of forsterite at 11 GPa – 1400^{o} C in the multianvil apparatus. Eur. J. Miner., 16: 877-889.

Debayle, E., Kennett, B., and Priestley, K. (2005). Global azimuthal seismic anisotropy and the unique plate-motion deformation of Australia. Nature, 433: 509-512.

Demouchy, S., Deloule, E., Frost, D.J., and Keppler, H. (2005). Pressure and temperature-dependence of water solubility in Fe-free wadsleyite. Am. Mineral., 90: 1084-1091.

Demouchy, S., Mainprice, D., Tommasi, A., Couvy, H., Barou, F., Frost, D.J., and Cordier, P. (2011). Forsterite to wadsleyite phase transformation under shear stress and consequences for the Earth's mantle transition zone. Phys. Earth. Planet. Inter., 184: 91-104.

Detrez, F., Castelnau, O., Cordier, P., Merkel, S., and Raterron, P. (2015). Effective viscoplastic behavior of polycrystalline aggregates lacking four independent slip systems inferred from homogenization methods: application to olivine. J. Mech. Phys. Solids, 83: 199-220.

Deuss, A. (2009). Global observations of mantle discontinuities using SS and PP precursors. Surv. Geophys., 30(4-5): 301-326.

Deuss, A. (2014). Heterogeneity and anisotropy of Earth's inner core. Annu. Rev. Earth Planet. Sci., 42: 103-126.

Duffy, T.S., Zha, C.S., Downs, R.T., Mao, H.K., and Hemley, R.J. (1995). Elasticity of forsterite to 16 GPa and the composition of the upper mantle. Nature, 387: 170-173.

Durinck, J., Legris, A., and Cordier, P. (2005) Pressure sensitivity of olivine slip systems: first-principle calculations of generalised stacking faults. Phys. Chem. Min., 32: 646-654.

Eakin, C.M., Long, M.D., Wagner, L.S., Beck, S.L., and Tavera, H. (2015). Upper mantle anisotropy beneath Peru from SKS splitting: constraints on flat slab dynamics and interaction with the Nazca Ridge. Earth Planet. Sci. Lett., 412: 152-162.

Estabrook, C.H and Kind, R. (1996). The nature of the 660-kilometer upper-mantle seismic discontinuity from precursors to the PP phase. Science, 274: 1179-1182.

Faul, U.H., Fitz Gerald, J.D., Farla, R.J.M., Ahlefeldt, R., and Jackson, I. (2011). Dislocation creep of fine-grained olivine. J. Geophys. Res.-Solid Earth, 116(B01203). Doi: 10.1029/2009JB007174.

Fischer, K.M. and Wiens, D.A. (1996). The depth distribution of mantle anisotropy beneath the Tonga subduction zone. Earth Planet. Sci. Lett., 142(1-2): 253-260.

Flanagan, M.P. and Shearer, P.M. (1998). Global mapping of topography on transition zone velocity discontinuities by stacking SS precursors. J. Geophys. Res., 103(B2): 2673- 2692.

Fouch, M.J. and Fischer, K.M. (1996). Mantle anisotropy beneath northwest Pacific subduction zones. J. Geophys. Res.-Solid Earth, 101(B7): 15987-16002.

French, S.W., and Romanowicz, B. (2015). Broad plumes rooted at the base of the Earth's mantle beneath major hotspots. Nature, 525: 95-99.

Fukao, Y., Obayashi, M., Inoue, H., and Nenbai, M. (1992). Subducting slabs stagnant in the mantle transition zone. J. Geophys. Res.-Solid Earth, 97(B4): 4809-4822.

Fukao, Y. and Obayashi, M. (2013). Subducted slabs stagnant above, penetrating through, and trapped below the 660 km discontinuity. J. Geophys. Res.-Solid Earth, 118(11): 5920-5938.

Gaherty, J.B. (2004). A surface wave analysis of seismic anisotropy beneath eastern North America. Geophys. J. Int., 158(3): 1053-1066.

Gu, Y.J., Okeler, A., and Schultz, R. (2012). Tracking slabs beneath northwestern Pacific subduction zones. Earth Planet. Sci. Lett., 331-332: 269-280.

Guest, W.S., and Kendall, J.M. (1993). Modelling seismic waveforms in anisotropic inhomogeneous media using ray and Maslov asymptotic theory: applications to exploration seismology. Can. J. Expl. Geophys., 29(1): 78-92.

Gwanmesia, G.D., Rigden, S., Jackson, I., and Liebermann, R.C. (1990). Pressure dependence of elastic wave velocity for beta-Mg_2SiO_4 and the composition of the Earth's mantle. Science, 250: 794-797.

Helffrich, G.R., and Wood, B.J. (1996). 410 km discontinuity sharpness and the form of the olivine α-β phase diagram resolution of apparent seismic contradictions. Geophys. J. Int., 126: F7-F12.

Hilairet, N., Wang, Y.B., Sanehira, T., Merkel, S., and Mei, S.M. (2012). Deformation of olivine under mantle conditions: an in situ high-pressure, high-temperature study using monochromatic synchrotron radiation. J. Geophys. Res., 117 (B01203). Doi: 10.1029/2011JB008498.

Hill, R. (1952). The elastic behaviour of a crystalline aggregate. Proc. Phys. Soc. London, Sect. A., 65(5): 349-354.

Inoue, T., Tanimoto, Y., Irifune, T., Suzuki, T., Fukui, H., and Ohtaka, O. (2004). Thermal expansion of wadsleyite, ringwoodite, hydrous wadsleyite and hydrous ringwoodite. Phys. Earth Planet. Inter., 143-144: 279-290.

Isaak, D.G. (1992). High-temperature elasticity of iron-bearing olivines. J. Geophys. Res.-Solid Earth, 97(B2): 1871-1885.

Isaak, D.G., Gwanmesia, G.D., Falde, D., Davis, M.G., Triplett, R.S., and Wang, L. (2007). The elastic properties of β-Mg_2SiO_4 from 295 to 660 K and implications on the composition of Earth's upper mantle. Phys. Earth Planet. Inter., 162(1-2): 22-31.

Jasbinsek, J. and Dueker, K. (2007). Ubiquitous low-velocity layer atop the 410-km discontinuity in the northern Rocky mountains. Geochem. Geophys. Geosyst., 8(10). Doi: 10.1029/2007GC001661.

Jung, H. and Karato, S. I. (2001a). Effects of water on dynamically recrystallized grain-size of olivine. J. Struc. Geol., 23: 1337-1344.

Jung, H., Katayama, I., Jiang, Z., Hiraga, T., and Karato, S. (2006). Effect of water and stress on the lattice-preferred orientation of olivine. Tectonophysics, 421(1-2): 1-22.

Jung, H., Mo, W., and Green, H.W. (2009). Upper mantle seismic anisotropy resulting from pressure-induced slip transition in olivine. Nature Geoscience, 2: 73-77.

Kaneshima, S. and Silver, P.G. (1992). A search for source side mantle anisotropy, Geophys. Res. Lett., 19(10): 1049-1052.

Karato, S. and Wu, P. (1993). Rheology of the upper mantle: a synthesis. Science, 260:771-778.

Katayama, I., Jung, H., and Karato, S. (2004). New type of olivine fabric from deformation experiments at modest water content and low stress. Geology, 32(12): 1045-1048.

Karato, S., Jung, H., Katayama, I., and Skemer, P. (2008). Geodynamic significance of seismic anisotropy of the upper mantle: new insights from laboratory studies. Ann. Rev. Earth Planet. Sci., 36: 59-95.

Katayama, I. and Karato, S. (2006). Effect of temperature on the B- to C-type olivine fabric transition and implication for flow pattern in subduction zones. Phys. Earth Planet. Int., 157(1-2): 33-45.

Katsura, T. and Ito, E. (1989). The system Mg_2SiO_4-Fe_2SiO_4 at high pressures and temperatures: precise determination of stabilities of olivine, modified spinel, and spinel. J. Geophys. Res.-Solid Earth, 94(B11): 15663:15670.

Katsura, T., Yamada, H., Nishikawa, O., Song, M., Kubo, A., Shinmei, T., Yokoshi, S., Aizawa, Y., Yoshino, T., Walter, M.J., Ito, E., and Funakoshi, K. (2004). Olivine-wadsleyite transition in the system $(Mg,Fe)_2Sio_4$. J. Geophys. Res.-Solid Earth, 109(B2). Doi: 10.1029/2003JB002438.

Kawasaki, I. and Konˈno, F. (1984). Azimuthal anisotropy of surface waves and the possible type of the seismic anisotropy due to preferred orientation of olivine in the uppermost mantle beneath the Pacific Ocean. J. Phys. Earth, 32: 229-244.

Kawazoe, T., Ohuchi, T., Nishihara, Y., Nishiyama, N., Fujino, K., and Irifune, T. (2013). Seismic anisotropy in the mantle transition zone induced by shear deformation of wadsleyite. Phys. Earth Planet. Int., 216: 91-98.

Kendall, J.M. (2000). Seismic anisotropy in boundary layers of the mantle. In: Karato, S., Forte, A.M., Liebermann, R.C., Masters, G., and Stixrude, L. (Eds.), Earth's deep interior: mineral physics and tomography from the atomic to the global scale, Geophys. Monogr. Ser., 117: 133-159, AGU, Washington DC, USA.

Kendall, J.M. and Silver P.G. (1998). Investigating causes of D″ anisotropy. In: Gurnis, M., Wysession, M.E., Knittle, E., and Buffett, B.A. (Eds.). The Core-Mantle Boundary Region. Geodyn. Ser., 28: 97-118. AGU, Washington DC, USA.

Kumazawa, M. and Anderson, O.L. (1969). Elastic moduli, pressure derivatives, and temperature derivatives of single-crystal olivine and single-crystal forsterite. J. Geophys. Res., 74(25): 5961-5972.

Lay, T., Williams, Q., Garnero E.J., Kellogg, L., and Wysession, M.E. (1998). Seismic wave anisotropy in the D″ region and its implications. In: Gurnis, M., Wysession, M.E., Knittle, E., and Buffett, B.A. (Eds.), The Core-Mantle Boundary Region. pp. 299-318. AGU, Washington DC, USA.

Lessing, S., Thomas, C., Rost, S., Cobden, L., and Dobson, D.P. (2014). Mantle transition zone structure beneath India and Western China from migration of PP and SS precursors. Geophys. J. Int., 197: 396-413.

Lessing, S., Thomas, C., Saki, M., Schmerr, N., and Vanacore, E. (2015). On the difficulties of detecting PP precursors. Geophys. J. Int., 201(3): 1666-1681.

Li, B., Liebermann, R.C., and Weidner, D.J. (1998). Elastic moduli of wadsleyite (β-Mg_2SiO_4) to 7 gigapascals and 873 Kelvin. Science, 281: 675-677.

Li, B., Liebermann, R.C., and Weidner, D.J. (2001). P-V-V_P-V_S-T measurements on wadsleyite to 7 GPa and 873 K: Implications for the 410-km seismic discontinuity. J. Geophys. Res., 106(B12): 30575-30591.

Liu, W., Kung, J., and Li, B. (2005). Elasticity of San Carlos olivine to 8 GPa and 1073 K. Geophys. Res. Lett., 32(16). Doi: 10.1029/2005GL023453.

Liu, W., Kung, J., Li, B., Nishiyama, N., and Wang, Y. (2009). Elasticity of $(Mg_{0.87}Fe_{0.13})_2SiO_4$ wadsleyite to 12 GPa and 1073 K. Phys. Earth and Planet. Int.,174: 98–104.

Long, M.D. (2009). Complex anisotropy in D″ beneath the eastern Pacific from SKS-SKKS splitting discrepancies. Earth Planet. Sci. Lett., 283: 181-189.

Long, M.D. and Silver, P.G. (2009). Shear wave splitting and mantle anisotropy: measurements, interpretations, and new directions. Surv. Geophys., 30(4-5): 407-461.

Long, M.D. and van der Hilst, R.D. (2005). Upper mantle anisotropy beneath Japan from shear wave splitting. Phys. Earth Planet. Int., 151: 206-222.

Mainprice, D. (2007). Seismic anisotropy of the deep Earth from a mineral and rock physics perspective. In: Schubert, G. (Ed.), Treatise on Geophysics, 2: 437- 492. Elseiver Oxford, UK.

Mainprice, D., Barruol, G., and Ben Ismaïl, W. (2000). The seismic anisotropy of the Earth's mantle: from single crystal to polycrystal, In: Karato, S.I., Forte, A., Liebermann R., Masters, G., Stixrude , L. (Eds.), Earth's deep interior: mineral physics and tomography from the atomic to global scale, Geophys. Monogr. Ser.,117: 237-264. AGU, Washington DC, USA.

Mainprice, D. and Silver, P.G. (1993). Interpretation of SKS-waves using samples from the subcontinental lithosphere. Phys. Earth Planet. Int., 78(3-4): 257-280.

Mainprice, D., Tommasi, A., Couvy, H., Cordier, P., and Frost, D. (2005). Pressure sensitivity of olivine slip systems and seismic anisotropy of Earth's upper mantle. Nature, 433: 731-733.

Mao, Z., Fan, D., Lin, J., Yang, J., Tkachev, S.N., Zhuravlev, K., and Prakapenka, V.B. (2015). Elasticity of single-crystal olivine at high pressures and temperatures. Earth Planet. Sci. Lett., 426: 204-215.

Mao, Z., Jacobsen, S.D., Jiang, F., Smyth, J.R., Holl, C.M., and Duffy, T.S. (2008b). Elasticity of hydrous wadsleyite to 12 GPa: Implications for Earth’s transition zone. Geophys. Res. Lett., 35(L21305). Doi: 10.1029/2008GL035618.

Mao, Z., Jacobsen, S.D., Jiang, F., Smyth, J.R., Holl, C.M., Frost, D.J., and Duffy, T.S. (2008a). Single-crystal elasticity of wadsleyite, β-Mg_2SiO_4, containing 0.37-1.66 wt% H_2O. Earth Planet. Sci. Lett., 268: 540-549.

Maupin, V., and Park, J. (2007). Theory and observations-wave propagation in anisotropic media, in Treatise on Geophysics, vol., 1, edited by Schubert, G, pp. 289-321. Elsevier, Amsterdam, Boston.

Mayama, N., Suzuki, I., Saito, T., Ohno, I., Katsura, T., Yoneda, A. (2004). Temperature dependence of elastic moduli of β-$(Mg,Fe)_2SiO_4$. Geophys. Res. Lett., 31(4). Doi: 10.1029/2003GL019247.

McNamara, A.K., van Keken, P.E., and Karato, S-I. (2003). Development of finite strain in the convecting lower mantle and its implications for seismic anisotropy. J. Geophys. Res., 108(B5). Doi: 10.1029/2002JB001970.

Mohiuddin, A., Long, M.D., and Lynner, C. (2015). Mid-mantle seismic anisotropy beneath southwestern Pacific subduction systems and implications for mid-mantle deformation. Phys. Earth Planet. Int., 245: 1-14.

Montagner, J.P. (1998). Where can seismic anisotropy be detected in the Earth's mantle? In boundary layers …, Pure Appl. Geophys., 151(2-4): 223-256.

Montagner, J.P. and Kennett, B.L.N. (1996). How to reconcile body-wave and normal-mode reference Earth models? Geophys. J. Int., 125(1): 229-248.

Morelli, A., Dziewonski, A.M., and Woodhouse, J.H. (1986). Anisotropy of the inner core inferred from PKIKP traveltimes. Geophys. Res. Lett., 13(13):1545-1548.

Müller, G. (1985). The reflectivity method: a tutorial. J. Geophys. Zeitsch. f. Geophys., 58 (1-3): 153-174.

Nicolas, A. and Christensen, N.I. (1987). Formation of anisotropy in upper mantle peridotites: A review. In: Fuchs, K. and Froidevaux, C. (Eds.), Composition, structure and dynamics of the lithosphere-asthenosphere system, Geodyn. Ser., 16: 111-123. AGU, Washington DC, USA.

Nippress, S.E.J., Kusznir, N.J., and Kendall, J.-M. (2004). Modeling of lower mantle seismic anisotropy beneath subduction zones. Geophys. Res. Lett., 31(L19612). Doi: 10.1029/2004GL020701.

Niu, F. and Chen, Q.- F. (2008). Seismic evidence for distinct anisotropy in the innermost inner core. Nature Geoscience, 1: 692-696.

Nowacki, A., Wookey, J., and Kendall, J.-M. (2010). Deformation of the lowermost mantle from seismic anisotropy. Nature, 467: 1091-1094.

Núñez-Valdez, M., da Silveira, P., and Wentzcovitch, R.M. (2011). Influence of iron on the elastic properties of wadsleyite and ringwoodite. J. Geophys. Res.-Solid Earth, 116 (B12). Doi: 10.1029/2011JB008378.

Núñez-Valdez, M., Wu, Z., Yu, Y.G., and Wentzcovitch, R.M. (2013). Thermal elasticity of $(Fe_x ,Mg_{1-x})_2SiO_4$ olivine and wadsleyite. Geophys. Res. Lett., 40(2): 290–294.

Ohuchi, T., Fujino, K., Kawazoe, T., and Irifune, T. (2014). Crystallographic preferred orientation of wadsleyite and ringwoodite: effects of phase transformation and water on seismic anisotropy in the mantle transition zone. Earth Planet. Sci. Lett., 397: 133-144.

Ohuchi, T., Kawazoe, T., Higo, Y., and Suzuki, A. (2017). Flow behavior and microstructures of hydrous olivine aggregates at upper mantle pressures and temperatures. Contrib. Mineral. Petrol. 172: :65. Doi: 10.1007/s00410-017-1375-8.

Ohuchi, T., Kawazoe, T., Nishihara, Y., Nishiyama, N., and Irifune, T. (2011). High pressure and temperature fabric transitions in olivine and variations in upper mantle seismic anisotropy. Earth Planet. Sci. Lett., 304(1-2): 55-63.

Ohuchi, T., Kawazoe, T., Higo, Y., Funakoshi, K.-I., Suzuki, A., Kikegawa, T., and Irifune, T. (2015). Dislocation-accommodated grain boundary sliding as the major deformation mechanism of olivine in the Earth's upper mantle. Sci. Adv. 1(9), e1500360. Doi: 10.1126/sciadv.1500360.

Pacalo, R.E.G., and Weidner, D.J. (1997). Elasticity of majorite, $MgSiO_3$ tetragonal garnet. Phys. Earth Planet. Int., 99: 145-154.

Panning, M. and Romanowicz, B. (2006). A three-dimensional radially anisotropic model of shear velocity in the whole mantle. Geophys. J. Int., 167: 361-379.

Ponte Castañeda, P. (2002) Second-order homogenization estimates for nonlinear composites incorporating field fluctuations. I—theory. J. Mech. Phys. Solids, 50(4):737–757.

Raterron, P., Chen, J., Li, L., Weidner, D., and Cordier, P. (2007). Pressure-induced slip-system transition in forsterite: Single-crystal rheological properties at mantle pressure and temperature. Am. Mineral., 92(8-9): 1436-1445.

Raterron, P., Detrez, F., Castelnau, O., Bollinger, C., Cordier, P., and Merkel, S. (2014). Multiscale modeling of upper mantle plasticity: from single-crystal rheology to multiphase aggregate deformation. Phys. Earth Planet. Int., 228: 232-243.

Ritsema, J. (2000). Evidence for shear velocity anisotropy in the lowermost mantle beneath the Indian Ocean. Geophys. Res. Lett., 27(7): 1041-1044.

Ritterbex, S., Carrez, P., and Cordier, P. (2016). Modeling dislocation glide and lattice friction in Mg_2 SiO_4 wadsleyite in conditions of the Earth's transition zone. Am. Mineral., 101(9): 2085-2094.

Rosa, A. D., Hilairet, N., Ghosh, S., Perrillat, J.-P., Garbarino, G., and Merkel, S. (2016). Evolution of grain sizes and orientations during phase transitions in hydrous Mg_2SiO_4. J. Geophys. Res., Solid Earth, 121: 7161-7176.

Rost, S., and Thomas, C. (2002). Array seismology: methods and applications. Rev. Geophys., 40(3): 2-1 – 2-27. Doi: 10.1029/2000RG000100.

Sawamoto, H., Weidner, D.J., Sasaki, S., and Kumazawa, M. (1984). Single-crystal elastic properties of the modified spinel (Beta) phase of magnesium orthosilicate. Science, 224: 749-751.

Saki, M., Thomas, C., Nippress, S., and Lessing, S. (2015). Topography of upper mantle seismic discontinuities beneath the North Atlantic: The Azores, Canary and Cape Verde plumes. Earth Planet Sci. Lett., 409: 193-202.

Savage, M.K. (1999). Seismic anisotropy and mantle deformation: what have we learned from shear wave splitting? Rev. Geophys., 37(1): 65-106.

Schmerr, N. and Garnero, E. (2006). Investigation of upper mantle discontinuity structure beneath the central Pacific using SS precursors. J. Geophys. Res.-Solid Earth, 111(B8). Doi: 10.1029/2005JB004197.

Schmerr, N. and Thomas, C. (2011). Subducted lithosphere beneath the Kuriles from migration of PP precursors. Earth Planet. Sci. Lett., 311: 101-111.

Shearer, P.M. (2000). Upper mantle seismic discontinuities. In: Karato, S., Forte, A., Liebermann, R., Masters, G., and Stixrude, L. (Eds.), Earth’s Deep Interior: Mineral Physics and Tomography from the Atomic to the Global Scale. Geophys. Monogr., Ser., 117: 115-131. AGU, Washington D.C., USA.

Silver, P.G. (1996). Seismic anisotropy beneath the continents: probing the depths of geology. Annu. Rev. Earth Planet. Sci., 24: 385-432.

Silver, P.G. and Chan, W.W. (1991). Shear wave splitting and subcontinental mantle deformation. J. Geophys. Res.-Solid Earth, 96(B10): 16429-16454.

Sinogeikin, S.V., Katsura, T., and Bass, J.D. (1998). Sound velocities and elastic properties of Fe-bearing wadsleyite and ringwoodite. J. Geophys. Res., 103(B9): 20819-20825.

Skemer, P., Warren, J.M., Kelemen, P.B. and Hirth, G. (2010). Microstructural and rheological evolution of a mantle shear zone. J. Petrol. 51(1-2): 43-53.

Smyth, J.R., Miyajima, N., Huss, G. R., Hellebrand, E., Rubie, D. C., and Frost, D. J. (2012). Olivine-wadsleyite-pyroxene topotaxy: Evidence for coherent nucleation and diffusion-controlled growth at the 410-km discontinuity. Phys. Earth Planet. Inter., 200: 85-91.

Song, X. (1996). Anisotropy in central part of inner core. J., Geophys. Res.-Solid Earth, 101(B7): 16089-16097.

Stammler, K. (1993). Seismic Handler: programmable multichannel data handler for interactive and automatic processing of seismological analysis. Comput. Geosci. 19: 135-140.

Stein, S. and Wysession, M. (2003). Introduction to seismology, Earthquakes, and Earth structure. Blackwell pub., Oxford.

Thomas, C. and Billen, M.I. (2009). Mantle transition zone structure along a profile in the SW Pacific: thermal and compositional variations. Geophys. J. Int., 176(1): 113-125.

Thomas, C. and Kendall, J.-M. (2002). The lowermost mantle beneath northern Asia-II. Evidence for lower-mantle anisotropy. Geophys. J. Int., 151(1): 296-308.

Thomas, C., Wookey, J., Brodholt, J., and Fieseler, T. (2011). Anisotropy as cause for polarity reversals of D'' reflections. Earth Planet. Sci. Lett., 307(3-4): 369-376.

Thurel, E., Cordier, P., Frost, D., and Karato, S.I. (2003a). Plastic deformation of wadsleyite: II. High-pressure deformation in shear. Phys. Chem. Min., 30(5): 267-270.

Thurel, E., Douin, J., and Cordier, P. (2003b). Plastic deformation of wadsleyite: III. Interpretation of dislocations and slip systems. Phys. Chem. Min., 30(5): 271-279.

Tommasi. A. (1998). Forward modeling of the development of seismic anisotropy in the upper mantle. Earth Planet. Sci. Lett., 160: 1-13.

Tommasi, A., Mainprice, D., Cordier, P., Thoraval, C., and Couvy, H. (2004). Strain-induced seismic anisotropy of wadsleyite polycrystals and flow patterns in the mantle transition zone. J. Geophys. Res, 109(B12). Doi: 10.1029/2004JB003158.

Tong, C., Gudmundsson, O., and Kennett, B.L.N. (1994). Shear wave splitting in refracted waves returned from the upper mantle transition zone beneath northern Australia. J. Geophys. Res.-Solid Earth, 99(B8): 15783-15797.

Trampert, J. and van Heijst, H.J. (2002). Global azimuthal anisotropy in the transition zone. Science, 296: 1297-1299.

van der Hilst, R., Engdahl, R., Spakman, W., and Nolet, G. (1991). Tomographic imaging of subducted lithosphere below northwest Pacific island arcs. Nature, 353: 37-43.

Visser, K., Trampert, J., Lebedev, S., and Kennett, B. L. N. (2008). probability of radial anisotropy in the deep mantle, Earth Plnaet. Sci. Lett., 270(3-4): 241-250.

Walker, A.M. and Wookey, J.M. (2012). MSAT- A new toolkit for the analysis of elastic and seismic anisotropy. Comput. Geosci., 49: 81-90.

Wang, J., Bass, J.D., and Katsura, T. (2014). Elastic properties of iron-bearing wadsleyite to 17.7 GPa: implications for mantle mineral models. Phys. Earth Planet. Int., 228: 92-96.

Warren, J.M. and Hirth, G. (2006). Grain size sensitive deformation mechanisms in naturally deformed peridotites. Earth Planet. Sci. Lett., 248(1-2): 438-450.

Wookey, J. and Kendall, J.M. (2004). Evidence of midmantle anisotropy from shear wave splitting and the influence of shear-coupled P waves. J. Geophys. Res.-Solid Earth, 109(B7). Doi: 10.1029/2003JB002871.

Wookey, J., Kendall, J.-M. and Barruol, G. (2002). Mid-mantle deformation inferred from seismic anisotropy. Nature, 415: 777-780.

Yu, Y., Park, J., and Wu, F. (1995). Mantle anisotropy beneath the Tibetan Plateau: evidence from long-period surface waves. Phys. Earth Planet. Int., 87(3-4): 231-246.

Yuan, K. and Beghein, C. (2013). Seismic anisotropy changes across upper mantle phase transitions. Earth Planet. Sci. Lett., 374: 132-144.

Yuan, H. and Romanowicz, B. (2010). Lithospheric layering in the North American craton. Nature, 466: 1063-1068.

Zha, C.S., Duffy, T.S., Downs, R.T., Mao, H.K., and Hemley, R.J. (1996). Sound velocity and elasticity of single-crystal forsterite to 16 GPa. J. Geophys. Res.-Solid Earth, 101(B8): 17535-17545.

Zha, C.S., Duffy, T.S., Downs, R.T., Mao, H.K., and Hemley, R.J. (1998). Brillouin scattering and X-ray diffraction of San Carlos olivine: direct pressure determination to 32 GPa. Earth Planet. Sci. Lett., 159: 25-33.

Zha, C.S., Duffy, T.S., Mao, H.K., Downs, R.T., Hemley, R.J., and Weidner, D.J. (1997). Single-crystal elasticity of β-Mg_2SiO_4 to the pressure of the 410 km seismic discontinuity in the Earth's mantle. Earth Planet. Sci. Lett., 147(1-4): E9-E15.

Zhang, J.S., and Bass, J.D. (2016). Sound velocities of olivine at high pressures and temperatures and the composition of Earth's upper mantle. Geophys. Res. Lett., 43: 9611-9618.

Zhang, S. and Karato, S.I. (1995). Lattice-preferred orientation of olivine aggregates in simple shear. Nature, 375: 774-777.

Zhang, S., Karato, S.I., Gerald, J.F., Faul, U.H., and Zhou, Y. (2000). Simple shear deformation of olivine aggregates. Tectonophysics, 316(1-2): 133-152.

Zheng, Z., and Romanowicz, B. (2012). Do double 'SS precursors' mean double discontinuities? Geophys. J. Int., 191: 1361-1373.

Zoeppritz, K. (1919). On the reflection and penetration of seismic waves through unstable layers. In: Göttinger Nachr., 1,66-84.

Figure 1: Schematic cartoon illustrating the effect of aligned minerals on the amplitude and polarity of the observed signals reflected off the 410 discontinuity, in different directions. This case describes an anisotropic layer of olivine which produces variable velocities in different directions (v1and v2), above an isotropic layer of wadsleyite with the same velocity in all directions (v3). The variation of velocity in different directions in the layer above give rise to variable amplitudes and perhaps polarities (indicated by the two waveforms).The dashed line shows the $P^{410}P/S^{410}S$ path. The orange arrow represents the direction of deformation/shear that aligns the crystals above the 410 km discontinuity.

Figure 2: Textures and predicted reflection coefficients for P and S waves as a function of azimuth. The reflection coefficients are modeled for P-P and SH-SH waves reflected off the underside of the 410 km discontinuity. The textures are calculated using the plastic model of olivine of Raterron et al. (2014) at 405 km assuming vertical compression, perpendicular to the 410 km discontinuity. a) Macroscopic deformation in compression, with compression direction along the Z axis. b) Axes reference used for displaying textures in this Figure and in the following figures. c) Olivine textures displayed for a random starting polycrystal (top row) and after 100% deformation (bottom row) in axial compression. The left, central and right panels show distribution probability for the orientation of axes [100], [010] and [001] in stereographic projection. d) P-P and SH-SH reflection coefficients as a function of azimuth (thick black curve) for starting texture (non-deformed) (top row) and after 100% axial deformation (bottom row) of the olivine layer. The reflection coefficients are calculated for P-P and SH-SH waves at an incident angle of 45^o. . The reflection coefficient diagrams are colour

coded, blue and red areas indicate positive and negative reflection coefficients respectively. The thin black lines represent the size of the reflection coefficients plotted with the increment of 0.05, ranging from 0 to +0.1 for the positive reflection coefficients and from -0.l to 0 for the negative ones. The size of the reflection coefficients are measured from the zero line between the positive (blue color) and negative area (red color).e) P wave (top panel) and S wave (bottom panel) reflection coefficients (solid circles) for different levels of deformation displayed over the incidence angle range of 15 to 65 degrees. Different levels of deformation are colour coded: white: starting texture, 25%, 50%, 75% and 100% axial deformation are shown by green, blue, yellow and red colours. Black dashed and solid curves represent the fitted polynomial to the values of the SH-SH reflection coefficients for the starting texture and the case of 100% axial deformation, respectively. The distance values corresponding to the critical incidence angle where the polarity reversal occurs are marked for the starting texture (vertical black dashed line) and for the maximum case of 100% applied deformation (vertical black solid line). The epicentral distances that correspond to the incidence angles at the 410 km discontinuity are marked by blue vertical dashed lines. Note that distances for the angles of incidence differ for P and S-waves.

Figure 3: Comparison of the textures calculated using two olivine plastic models taken from the study of Raterron et al. (2014), at the conditions of 405 km depth, with dominant slip along [001](010) and that of Tommasi (1998) with dominant slip on [100](010). a) Horizontal shear deformation, shear direction along X axis with Z axis normal to the shear plane. b) Pole figures representing textures for γ(shear strain)=2 (top row) and γ=4(bottom row) for olivine polycrystals for the model of Raterron et al. (2014). (c) Same as (b) but for the model of Tommasi (1998). The left, central and right panels in each section show distribution probability of the orientations of axes [100], [010] and [001] in stereographic projection.

Figure 4: Comparison of the textures calculated for deformation in axial compression using two olivine plastic models taken from the study of a) Raterron et al. (2014), at the conditions of 405 km depth, with dominant slip along [001](010) and b) that of Tommasi (1998) with dominant slip on [100](010). Pole figures representing textures for the case of 100% imposed deformation. The left,

central and right panels in each section show distribution probability for the orientation of axes [100], [010] and [001] in stereographic projection.

Figure 5: Predicted reflection coefficients of P and S waves reflected off the underside of the 410 km discontinuity when olivine is deformed in horizontal shear as a function of azimuth and using suggested dominant slip system of olivine taken from the study of Raterron et al. (2014). a) P-P and SH-SH reflection coefficients (black curve) for isotropic case (top row) and γ=4.0 (bottom row). The incidence angle for these cases is 55 degrees. The blue and red colour and the thin black lines are the same as described in Figure 2.d. (b,c,d) P wave (left panel) and S waves (right panel) reflection coefficients (solid circles) for isotropic olivine and after γ=4.0 deformation displayed over the incidence angle range of 15 to 65 degrees for the cases of azimuths parallel (b), 45 degrees (c) and perpendicular (d) to the direction of deformation. Different levels of deformations are colour coded: starting texture and γ=4.0 are shown by white and red circles, respectively. Dashed and solid curves represents the fitted polynomials to the values of the SH-SH reflection coefficients for the cases of the isotropic model and γ=4.0, respectively. The distance value corresponding to the incidence angle where the polarity reversal occurs are shown for the isotropic case (vertical dashed line) and for a shear strain of γ= 4.0 (vertical solid line).

Figure 6: Comparison of the S wave reflection coefficients for olivine deformed in horizontal and vertical shear using two different dominant slip systems for olivine. a) Predicted reflection coefficient of SH wave for a horizontal shear system (solid circles), modeled using Raterron et al. (2014) (R-14) plastic model of olivine shown for the incidence angle range of 15 to 65 degrees. b) SH wave reflection coefficient for a horizontal and vertical shear system displayed over the incidence angle range of 40 to 60 degrees using (R-14) and Tommasi (1998) (T-98) plastic models for olivine. Reflection coefficients are shown for the cases of azimuths parallel (top row), 45 degrees (middle row) and 90 degrees to the direction of deformation (bottom row) (horizontal shear) or normal to the shear plane (vertical shear).

Figure 7: Predicted reflection coefficients of P and S waves reflected off the 410 km discontinuity as a function of azimuth and using the dominant slip system of olivine taken from the study of Raterron et al. (2014). Olivine and wadsleyite are deformed in horizontal shear with shear strain of γ = 4.0 and γ =0.4, respectively. a) P wave (left panel) and S waves (right panel) reflection coefficients (solid circles) displayed over the incidence angle range of 15 to 65 degrees for three cases of : isotropic olivine and wadsleyite (white circles), deformed olivine with shear strain of γ =4.0 and isotropic wadselyite (red circles) and for deformed olivine with shear strain of γ =4.0 and wadsleyite with shear strain of γ =0.4 (blue circles). The reflection coefficients are shown for the azimuths parallel (a), 45 degrees (b) and perpendicular (c) to the direction of deformation. Fitted polynomials to the values of the SH-SH reflection coefficients are shown for the cases of the isotropic model (dashed), deformed olivine with γ =4.0 and isotropic wadsleyite (solid) and deformed olivine with γ =4.0 and wadsleyite with γ =0.4 (dashed-dotted). The distance value corresponding to the incidence angle where the polarity reversal occurs are shown for the isotropic case (vertical dashed line), deformed olivine (γ =4.0) and isotropic wadsleyite (vertical solid line) and deformed olivine (γ =4.0) and wadsleyite (γ =0.4) (vertical dashed-dotted line). The epicentral distances that correspond to the right most and left most vertical lines are indicated.

Figure 8: Synthetic vespagram (e.g., Rost and Thomas, 2002) for the transverse component of a synthetic event in 50 to 60 degrees distance and a depth of 50 km calculated using the reflectivity method (Müller, 1985). The synthetic seismograms are computed using the velocity model ak135. The arrival times and slowness values of the S, SS, SS precursors, ScS waves as well as their depth phases, predicted for ak135 are indicated.

Table 1: Elastic parameters for olivine and wadsleyite at 410 km depth. For olivine, we use the full set of anisotropic single-crystal elastic moduli based on available literature data of Mao et al. (2015). Here, wadsleyite is assumed to be isotropic due to the lack of available data at high temperature.

Table 2: Plastic models for olivine. Model 1 is adopted from Raterron et al. (2014) at 405 km depth and model 2 is from Tommasi (1998). For each, the table indicates the relative critical resolved shear

stresses (CRSS) of each plastic deformation mechanism as well as the relative activities of each deformation mode after 50% axial compression and at a shear strain of γ =1. For both plastic models, the CRSS of the isotropic relaxation mechanism was adjusted so that it accommodates 40 to 50% of the effective plastic activity. Stars indicate plastic modes that were not included in the simulation.

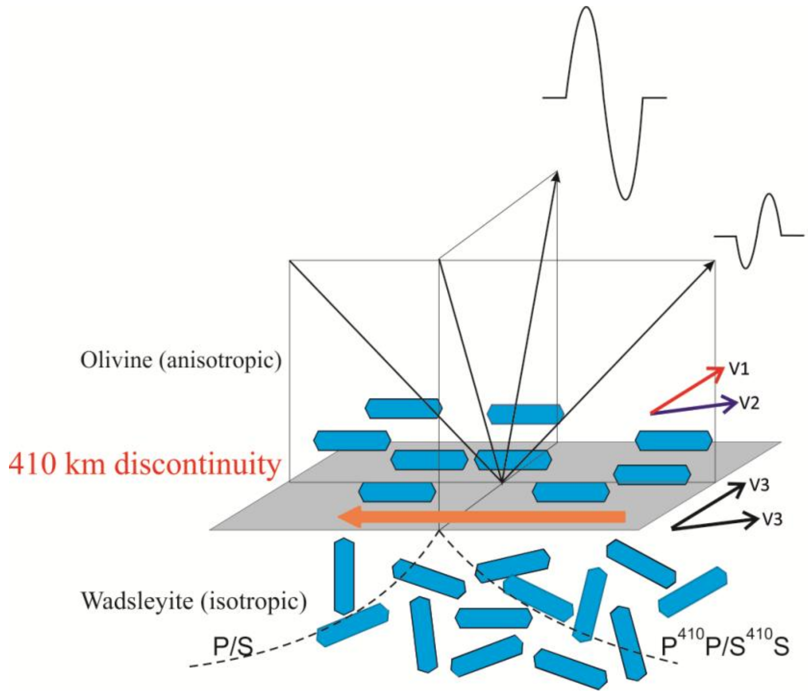

Figure 1

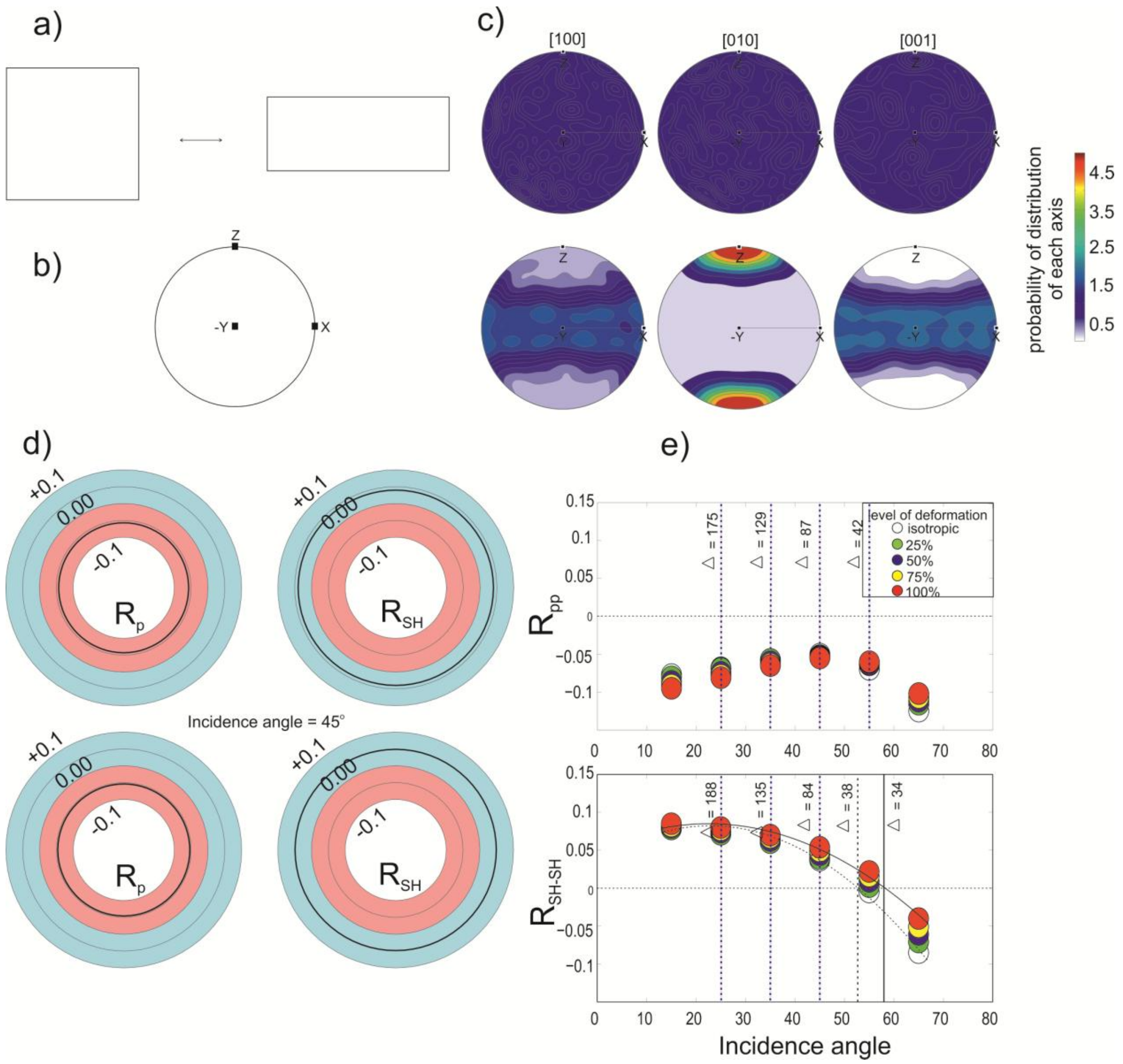
a)
b)
Z
-Y
X
c)
[100]
[010]
[001]
Z
-Y
X
probability of distribution of each axis
4.5
3.5
2.5
1.5
0.5
d)
+0.1
0.00
-0.1
R_p
R_{SH}
Incidence angle = 45°
e)
R_{pp}
R_{SH-SH}
level of deformation
isotropic
25%
50%
75%
100%
△ = 175
△ = 129
△ = 87
△ = 42
△ = 188
△ = 135
△ = 84
△ = 38
△ = 34
Incidence angle

Figure 2

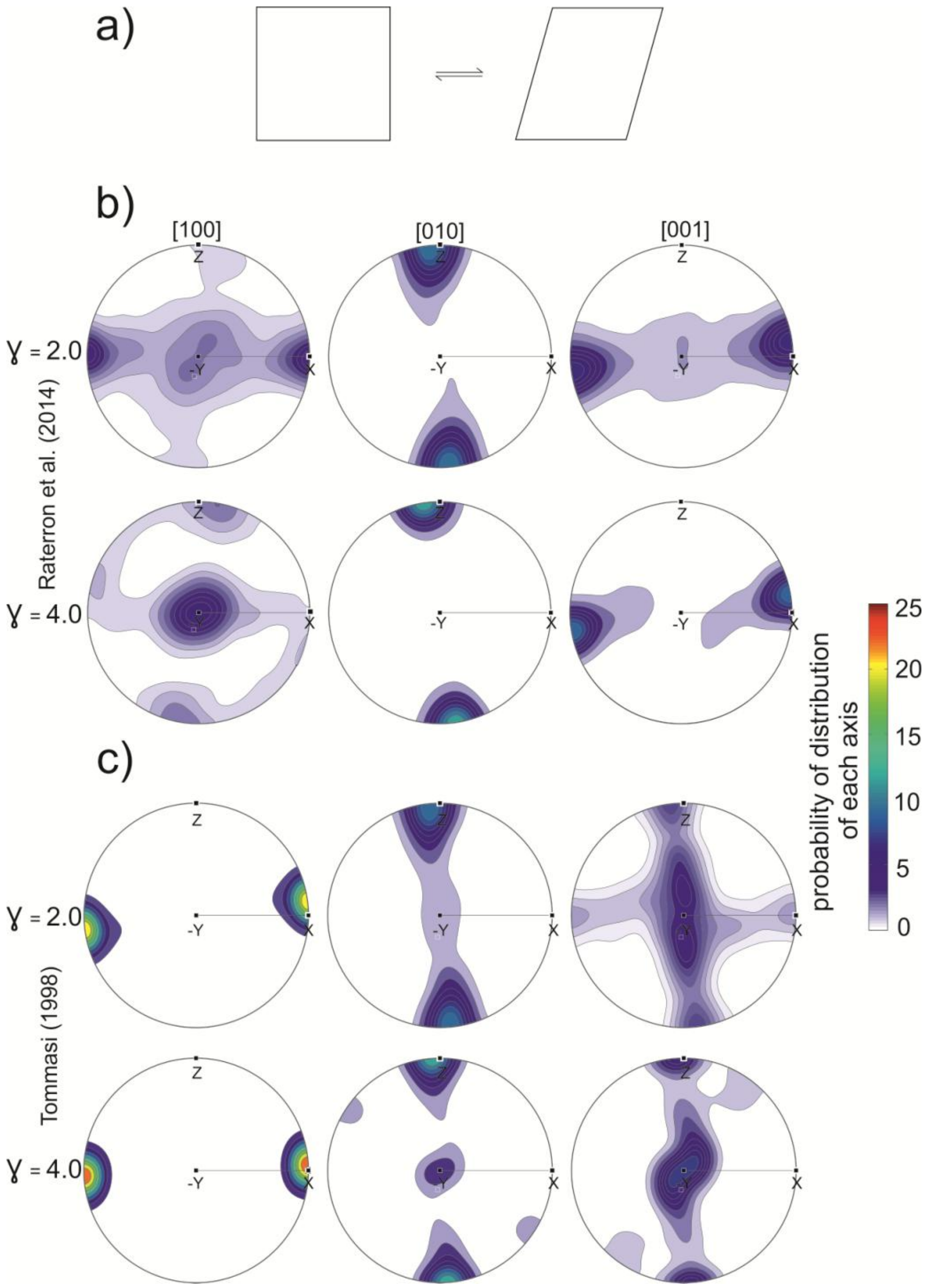

a)
b)
[100]
[010]
[001]
Z
-Y
X
γ = 2.0
γ = 4.0
Raterron et al. (2014)
c)
Tommasi (1998)
probability of distribution of each axis
0
5
10
15
20
25

Figure 3

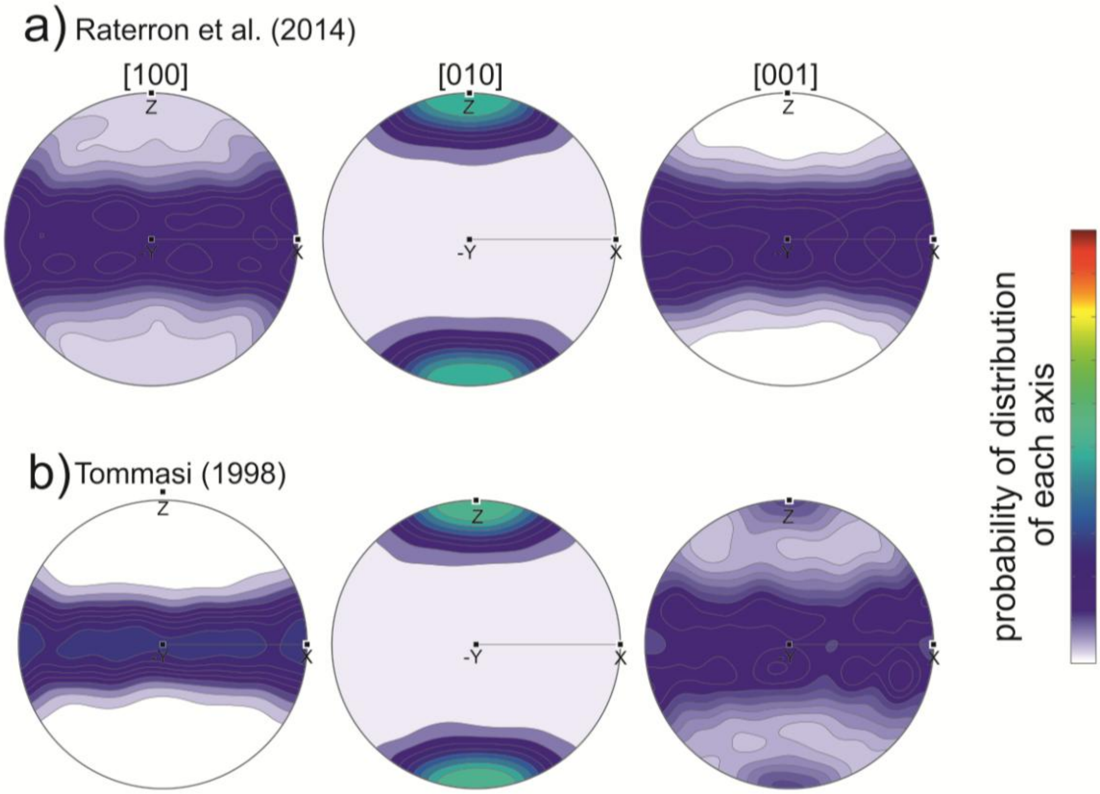
a) Raterron et al. (2014)
[100]
[010]
[001]
Z
-Y
X
b) Tommasi (1998)
probability of distribution
of each axis
9
7
5
3
1

Figure 4

981

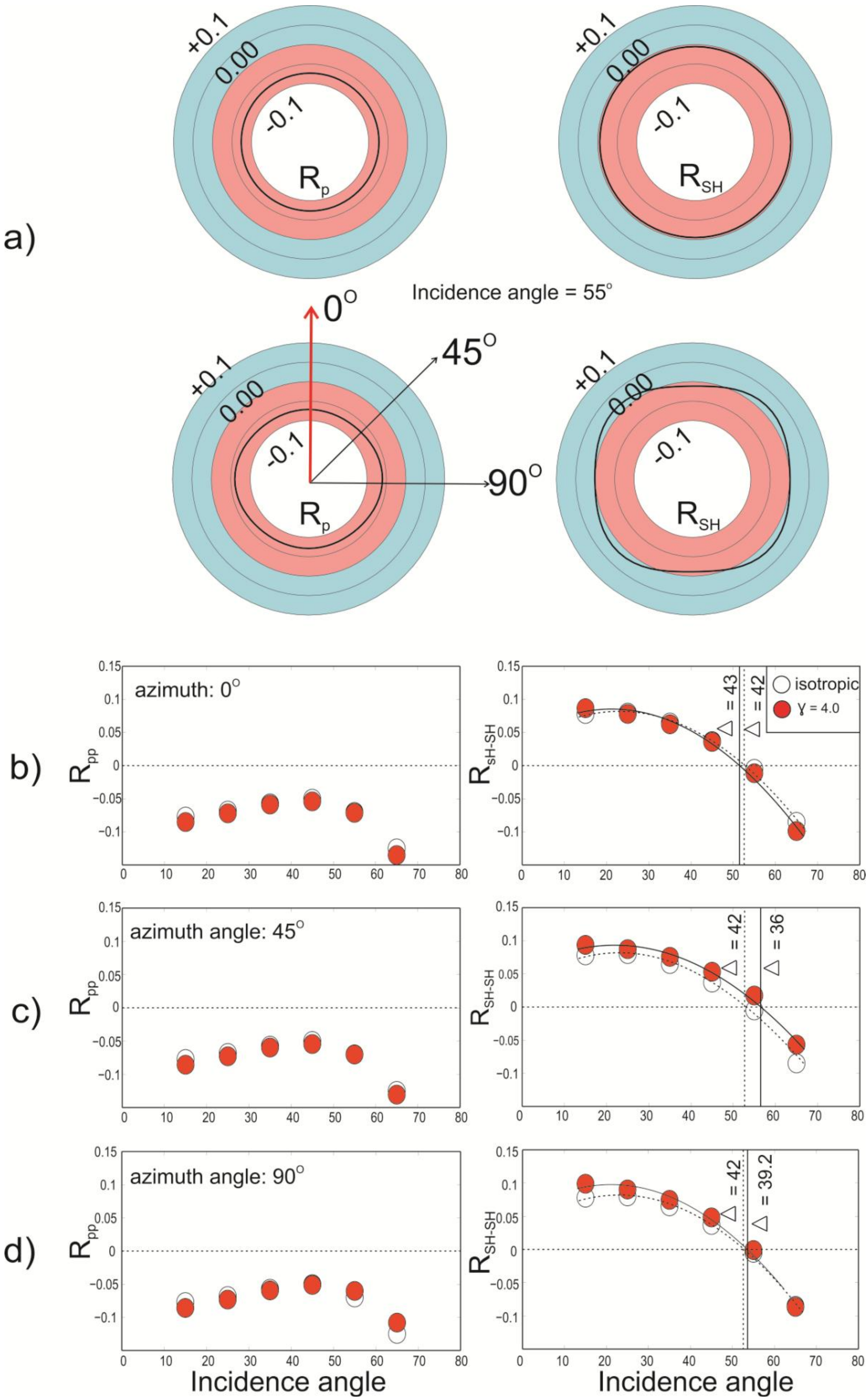
a)
+0.1
0.00
-0.1
R_p
R_{SH}
Incidence angle = 55°
0°
45°
90°
b)
azimuth: 0°
c)
azimuth angle: 45°
d)
azimuth angle: 90°
R_{pp}
R_{sH-SH}
R_{SH-SH}
isotropic
γ = 4.0
Δ = 43
Δ = 42
Δ = 36
Δ = 39.2
Incidence angle

Figure 5

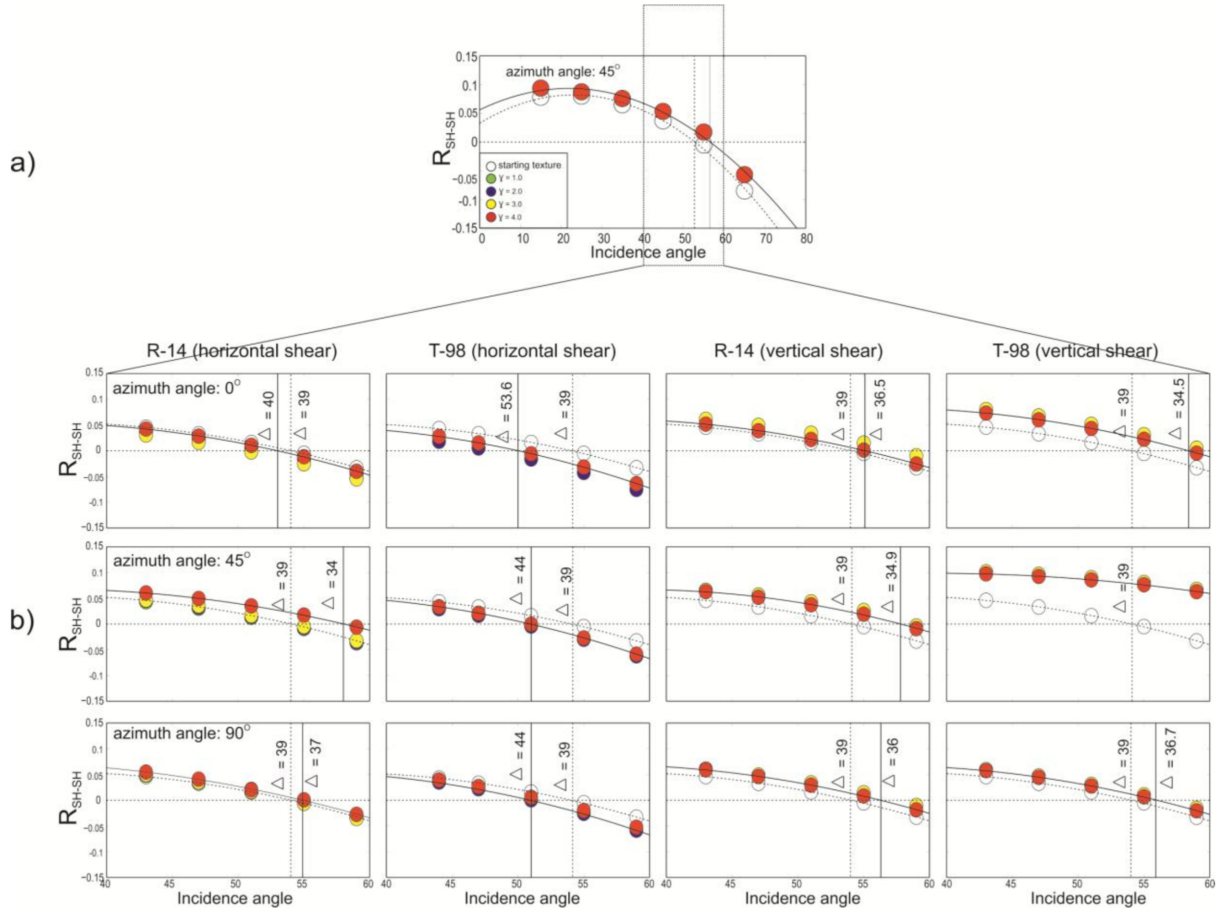

Figure 6

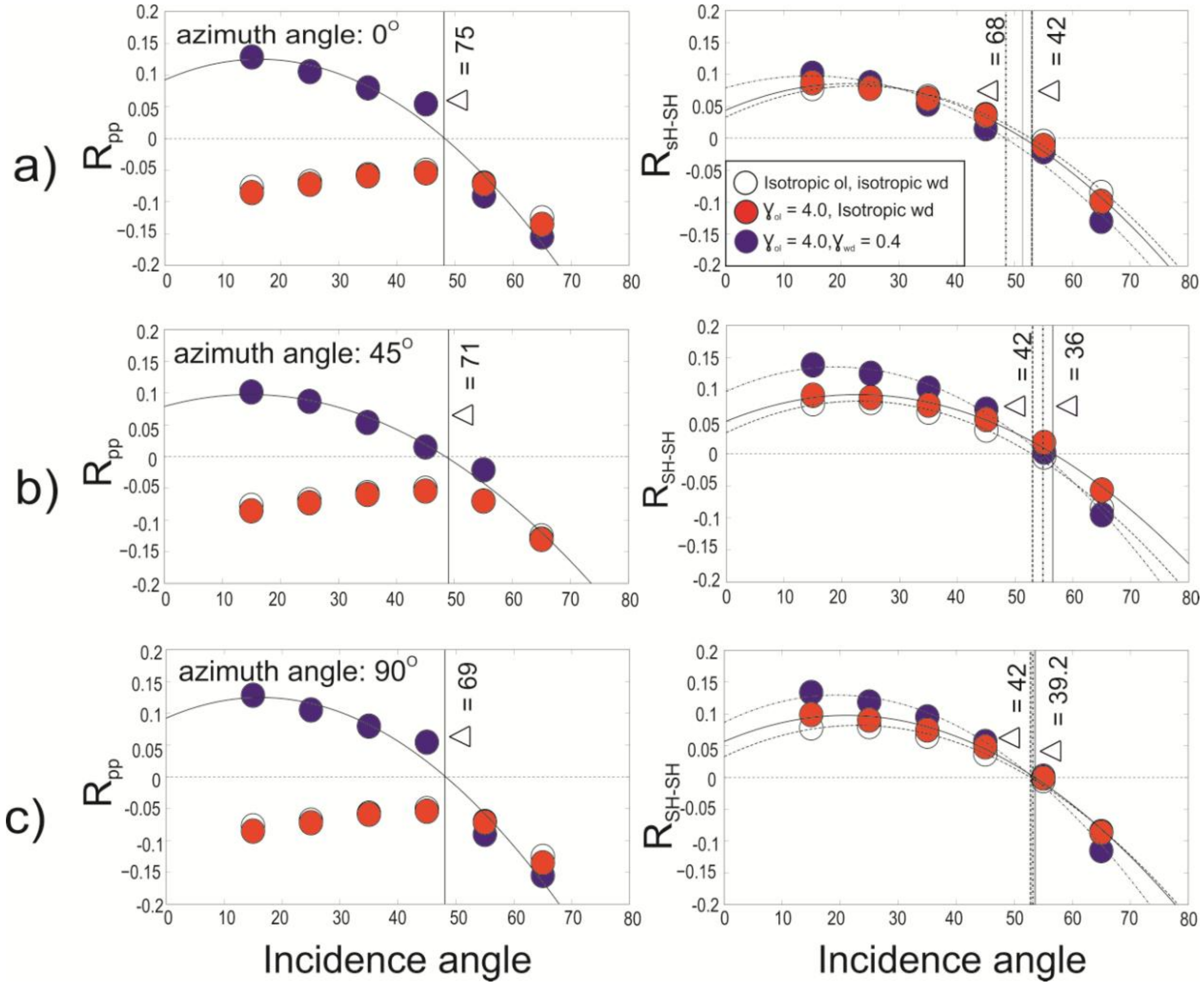
a)
b)
c)
R_pp
R_sH-SH
R_SH-SH
azimuth angle: 0°
azimuth angle: 45°
azimuth angle: 90°
Δ = 75
Δ = 68
Δ = 42
Δ = 71
Δ = 42
Δ = 36
Δ = 69
Δ = 42
Δ = 39.2
Isotropic ol, isotropic wd
γol = 4.0, Isotropic wd
γol = 4.0,γwd = 0.4
Incidence angle
Incidence angle

Figure 7

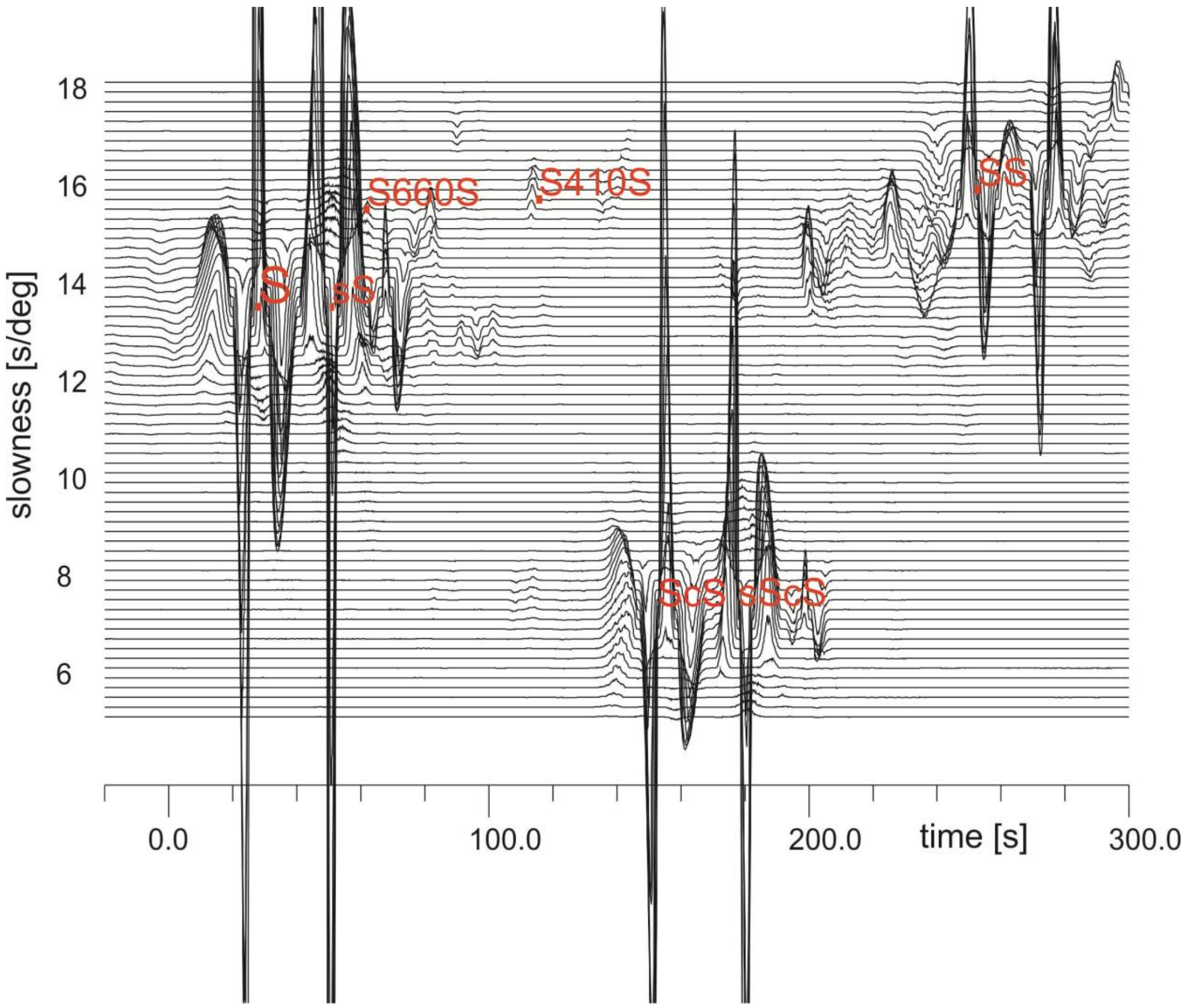

Figure 8

Table 1

C_{ij} (GPa)- ρ(g/cm^3)	Olivine (single-crystal)	Wadsleyite (single-crystal)
C_{11}	349	337
C_{22}	219	
C_{33}	250	
C_{44}	68	½(C_{11}-C_{12})
C_{55}	78	
C_{66}	75	
C_{12}	84	
C_{13}	93	130

C_{23}	98	
Density (ρ)	3.42	3.60

Table 2

	Model 1 (R-14)			Model 2 (T-98)		
Mechanism	CRSS	Effective activity		CRSS	Effective activity	
		Compression	Shear		Compression	Shear
[100](010)	42	9%	7%	10	20%	24%
[001](010)	15	25%	23%	20	25%	13%
[001](100)	46	2%	3%	30	1%	1%
[100](001)	56	1%	2%	10	14%	20%
[100]{011}	*	*	*	40	1%	1%
[100]{021}	42	14%	11%	*	*	*
[100]{031}	*	*	*	40	1%	1%
[001]{110}	45	5%	6%	60	0%	0%
Isotropic	200	44%	48%	150	39%	40%